Monthly Notices
of the
ROYAL ASTRONOMICAL SOCIETY

MNRAS **493,** 3656–3675 (2020)
Advance Access publication 2020 February 11

doi:10.1093/mnras/staa409

NGC 7469 as seen by MEGARA: new results from high-resolution IFU spectroscopy

S. Cazzoli [1]★ A. Gil de Paz,[2,3] I. Márquez [1] J. Masegosa,[1] J. Iglesias,[1] J. Gallego,[2,3] E. Carrasco,[4] R. Cedazo,[5] M. L. García-Vargas [6] Á. Castillo-Morales,[2,3] S. Pascual,[2,3] N. Cardiel,[2,3] A. Pérez-Calpena,[6] P. Gómez-Alvarez,[6] I. Martínez-Delgado[6] and L. Hermosa-Muñoz [1]

[1]*IAA - Instituto de Astrofísica de Andalucía (CSIC), Apdo. 3004, E-18008 Granada, Spain*
[2]*Departamento de Física de la Tierra y Astrofísica, Universidad Complutense de Madrid, E-28040 Madrid, Spain*
[3]*Instituto de Física de Partículas y del Cosmos IPARCOS, Facultad de Ciencias Físicas, Universidad Complutense de Madrid, E-28040 Madrid, Spain*
[4]*INAOE - Instituto Nacional de Astrofísica, Óptica y Electrónica, Luis Enrique Erro No.1, C.P. 72840 Tonantzintla, Puebla, Mexico*
[5]*Universidad Politécnica de Madrid, C.P. E-72840 Madrid, Spain*
[6]*Fractal, S.L.N.E., Madrid, Spain*

Accepted 2020 February 6. Received 2020 February 6; in original form 2019 September 12

ABSTRACT

We present our analysis of high-resolution ($R \sim 20\,000$) GTC/MEGARA integral-field unit spectroscopic observations, obtained during the commissioning run, in the inner region (12.5 arcsec × 11.3 arcsec) of the active galaxy NGC 7469, at spatial scales of 0.62 arcsec. We explore the kinematics, dynamics, ionization mechanisms, and oxygen abundances of the ionized gas, by modelling the Hα-[N II] emission lines at high signal-to-noise (> 15) with multiple Gaussian components. MEGARA observations reveal, for the first time for NGC 7469, the presence of a very thin (20 pc) ionized gas disc supported by rotation (V/σ = 4.3), embedded in a thicker (222 pc), dynamically hotter (V/σ = 1.3) one. These discs nearly corotate with similar peak-to-peak velocities (163 versus 137 km s^{-1}), but with different average velocity dispersion (38 ± 1 versus 108 ± 4 km s^{-1}). The kinematics of both discs could be possibly perturbed by star-forming regions. We interpret the morphology and the kinematics of a third (broader) component ($\sigma > 250$ km s^{-1}) as suggestive of the presence of non-rotational turbulent motions possibly associated either to an outflow or to the lense. For the narrow component, the [N II]/Hα ratios point to the star-formation as the dominant mechanism of ionization, being consistent with ionization from shocks in the case of the intermediate component. All components have roughly solar metallicity. In the nuclear region of NGC 7469, at $r \leq 1.85$ arcsec, a very broad (FWHM = 2590 km s^{-1}) Hα component is contributing (41 per cent) to the global Hα-[N II] profile, being originated in the (unresolved) broad line region of the Seyfert 1.5 nucleus of NGC 7469.

Key words: techniques: spectroscopic – galaxies: active – galaxies: ISM – galaxies: kinematics and dynamics.

1 INTRODUCTION

Long slit and multiobject spectroscopy have been traditionally used to obtain spectra for both point and extended sources. While both techniques are efficient for single and unresolved sources, spatially resolved spectroscopy is needed for an optimal study of extended resolved sources. Integral Field Spectroscopy (IFS) has the advantage of being able to provide a spectrum of a spatial element in a 2D field over a potentially long wavelength coverage. Nowadays, the number of integral field units (IFUs) is growing and many detailed studies of individual objects and large IFS surveys are being carried out (e.g. CALIFA, Sánchez et al. 2012; SAMI, Croom et al. 2012; MaNGA, Bundy et al. 2015; SINS, Förster Schreiber et al. 2009; KMOS-3D,Wisnioski et al. 2015). However, all these studies are limited by the spectral resolution (generally less than 6000). This limits the detection and the kinematic analysis of galaxy component that might be detected as rather narrow but blended

★ E-mail: sara@iaa.es

Table 1. General properties of NGC 7469.

Properties	Value	References
R.A.	$23^h03^m15^s.6$	–
Decl.	$+08^d52^m26^s$	–
z	0.016317	NED
Distance (Mpc)	70.2	NED
Scale (pc arcsec^{-1})	340	NED
Hubble classification	(R')SAB(rs)a	Galbany et al. (2016)
Activity	Sy1.5	Landt et al. (2008)
Log ($L_{IR}/L_\odot$)	11.7	Sanders et al. (2003)
SFR ($M_\odot$ yr^{-1})	48	Pereira-Santaella et al. (2011)
i (°)	30.2	Hyperleda
PA_{phot} (°)	126	Hyperleda

Note. 'Distance' and 'scale' are from the Local Group, as listed in the NASA Extragalactic Data base, NED. 'L_{IR}' corresponds to the L_{8-1000} and it is calculated using the fluxes in the four *IRAS* bands as given in Sanders et al. (2003). 'SFR' is the star-formation rate based on the 24 μm luminosity. The AGN contribution to the 24 μm luminosity is subtracted. The inclination position angle and 'i' and 'PA_{phot}', are defined as the inclination between line of sight and polar axis of the galaxy and the major axis position angle (north eastwards), respectively. More specifically, 'PA_{phot}' is the average value between the measurements from Paturel et al. (2000) and the 'Uppsala General Catalogue of Galaxies' (Nilson 1973) and i is determined from the axial ratio of the isophote in the *B*-band using a correction for intrinsic thickness based on the morphological type (see references in Hyperleda for individual measurements).

components. This is especially relevant for the Hα-[N II] complex, the most studied optical tracer, due to the proximity of the lines (15–20 Å). With the advent of MEGARA (*Multi-Espectrógrafo en GTC de Alta Resolución para Astronomía*; Gil de Paz et al. 2014, 2018; Carrasco et al. 2018) the new IFU at the 10.4 m Gran Telescopio Canarias (GTC) high spectral resolution (up to 20 000) IFS observations have become available. MEGARA started the operation in 2017 and during the commissioning run the NGC 7469 galaxy has been observed among others (e.g. NGC 7025 Dullo et al. 2019 and UGC 10205 Catalán-Torrecilla et al. 2020).

NGC 7469 (IRAS 23007 + 0836, MRK 1514) is a well-studied active galaxy in the local Universe ($z = 0.016317$). Table 1 summarizes the basic properties for this object and in Fig. 1 its optical morphology is shown from *Hubble Space Telescope* (*HST*) observations.

The Seyfert 1.5 nucleus of NGC 7469 (Landt et al. 2008) is hosted by a spiral galaxy (Fig. 1). NGC 7469 forms part of a galaxy pair together with IC 5283 at a projected distance of 60–70 Mpc (Marquez & Moles 1994). Their past interaction, occurred 1.5×10^8 yr ago (Genzel et al. 1995), is believed to have triggered the powerful star formation activity of NGC 7469 (SFR $= 48\,M_\odot$ yr^{-1}; Pereira-Santaella et al. 2011), mainly occurring in the circumnuclear star-forming ring bright at various wavelengths: radio (e.g. Colina et al. 2001; Davies, Tacconi & Genzel 2004), optical (e.g. Scoville et al. 2000; Colina et al. 2007) and infrared (e.g. Soifer et al. 2003; Díaz-Santos et al. 2007). Such prominent star formation activity along with an high IR-luminosity ($\log(L_{IR}/L_\odot) = 11.7$; Sanders et al. 2003) led NGC 7469 to be enclosed among Luminous Infrared Galaxies (LIRGs).

The spatially resolved disc kinematics has been studied mainly through ALMA and VLT/SINFONI observations of cold and warm molecular gas and ionized gas by different authors (Davies et al. 2004; Alonso-Herrero et al. 2009; Hicks et al. 2009; Fathi et al. 2015; Izumi et al. 2015). Briefly these works found that the velocity fields obtained from the modelling of HCN, CO, H_2 λ2.12 μm, Hα λ6563 and Brγ λ2.165 μm emission lines are suggestive of uniform large-scale rotation stable against star formation, with no indication of warps or bar. However, a lense is found to be relevant at distances between 5.0 and 15.0 arcsec from the nucleus (Marquez & Moles 1994).

Non-rotational motions, such as outflows are thought to be common in galaxies (Veilleux, Cecil & Bland-Hawthorn 2005 for a review). Growing evidence of outflows has been collected in the Milky Way (e.g. Fox et al. 2015, 2019; Bordoloi et al. 2017) and external galaxies, i.e. starbursts (e.g. Heckman et al. 2000; Chen et al. 2010; Westmoquette, Smith & Gallagher 2011), LIRGs (e.g. Arribas et al. 2014; Cazzoli et al. 2014, 2016; Pereira-Santaella et al. 2017) and AGNs (e.g. Harrison et al. 2014; Fiore et al. 2017; Maiolino et al. 2017; Cazzoli et al. 2018; Hernández-García et al. 2018) at any redshift. In the case of NGC 7469, Müller-Sánchez et al. (2011) found a wide angle nuclear outflow (half opening angle of

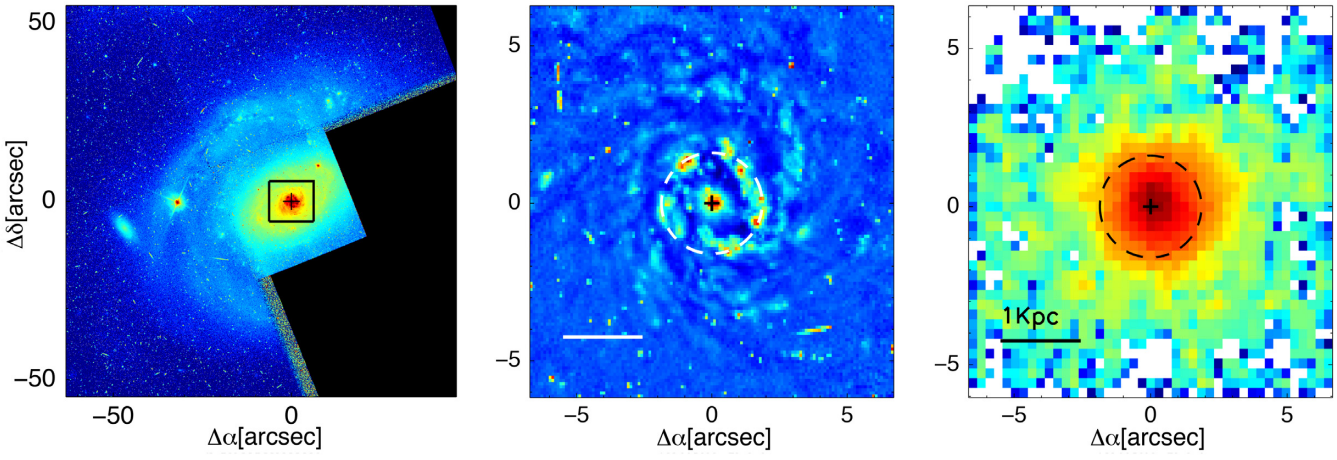

Figure 1. Optical images of NGC 7469. The left-hand panel shows the large-scale *HST*-WFPC2 image (F606W filter), whereas the middle panel displays its sharp-divided image (Section 2) with a zoomed-in view. The zoomed image matches the field of view of MEGARA observations marked with a black square in the left-hand panel. In the right-hand panel, the optical continuum from MEGARA IFU datacube (Section 2). In all panels, the cross marks the galaxy nucleus (i.e. the peak of the continuum emission, see also Section 2). Horizontal bars show a linear scale of 1 kpc (see Table 1). The dashed circles indicates the nuclear region (Section 2).

45°) with a (maximum) velocities $< 200\,\mathrm{km\,s^{-1}}$ by analysing [S IV] coronal line at 1.96 μm in the central 0.8 arcsec × 0.8 arcsec with SINFONI/VLT data. Evidence of the presence of a high velocity outflow ($V \geq 580\,\mathrm{km\,s^{-1}}$) are found at X-rays (Blustin et al. (2007) and reference therein).

In this paper, we used optical high spectral resolution ($R \sim 20\,000$) MEGARA/GTC IFS observations to investigate the presence of the multiple distinct kinematic components of the H α-[N II] λλ6548,6584 complex associated to disc kinematics or non-rotational motions (e.g. outflows and/or chaotic motions associated to the lense) in NGC 7469. Our main goals are to characterize all the components by studying their kinematics and dynamics, as well as exploring their possible dominant ionization mechanism and infer oxygen abundances. Furthermore, we aim at investigating the properties of H α broad component originated in the broad-line region (BLR) of the AGN of NGC 7469.

This paper is organized as follows. In Section 2, the data and observations are presented as well as the data reduction. In Section 3, we present the spectroscopic analysis: line modelling and maps generations. The details of the kinematic analysis are given in Section 4. In Section 5, the main observational results are highlighted. In Section 6, we discuss the origin, kinematics, dynamics, the ionization mechanisms and oxygen abundances of the different components considered in the line modelling. Finally, the main conclusions are presented in Section 7.

Throughout the paper we will assume $H_0 = 70\,\mathrm{km\,s^{-1}\,Mpc^{-1}}$ and the standard $\Omega_m = 0.3$, $\Omega_\Lambda = 0.7$ cosmology.

All images and spectral maps are oriented following the standard criterium so the north is up and east to the left.

2 OBSERVATIONS AND DATA REDUCTION

Observations were carried out with GTC/MEGARA on 2017 July 25 during the MEGARA commissioning run. The 567 fibres that constitute the MEGARA IFU (100 μm in core size) are arranged on a square microlens-array that projects on the sky a field of 12.5 arcsec × 11.3 arcsec in size. Each microlens is a hexagon inscribed in a circle with diameter of 0.62 arcsec projected in the sky. A total of 56 ancillary fibres (organized in eight fibre bundles), located at a distance of 1.75– 2.0 arcmin from the centre of the IFU field of view, deliver simultaneous sky observations.

We used the HR-R Volume-Phased Holographic (VPH, i.e. VPH665-HR) covering the 6405.6 – 6797.1 Å spectral range with a spectral resolution of $R \sim 20\,000$ (from 19 500 to 20 600). The linear dispersion is of ∼0.0974 Å per pixel hence $\sim 5\,\mathrm{km\,s^{-1}}$ at the corresponding wavelength of H α λ6563. We obtained three exposures of 600 s each to facilitate cosmic-rays removal. During the observations of NGC 7469 the dimm-seeing was 1.02 arcsec; airmass was 1.28.

MEGARA raw data were reduced with the data reduction package provided by Universidad Complutense de Madrid (MEGARA DRP;[1] version 0.8; Pascual et al. 2019a,b) following the MEGARA cookbook.[2] The pipeline allows us to perform the following steps: sky and bias subtraction, flat-field correction, spectra tracing and extraction, correction of fibre and pixel transmission, and wavelength calibration. We did not apply any flux calibration, as we are mainly interested in the kinematic analysis.

We apply a regularization grid to obtain square spaxels[3] of size of 0.31 arcsec; the final cube has dimensions of 43 × 40 × 4300, equivalent to a total of 1720 spectra in the datacube.

The point spread function (PSF) of the MEGARA datacube could be described as Moffat function (Moffat 1969) and it has been estimated to have a full width at half-maximum (FWHM) of 0.93 arcsec from the 2D profile brightness distribution of standard stars. Throughout the paper, in order to avoid any possible PSF contamination in the kinematic measurements, we will conservatively consider as 'nuclear region' a circular area of radius equal to the width at 5 per cent intensity of the PSF radial profile, i.e. 1.85 arcsec (see Fig. 1). This area nearly coincides with the outer radius of the circumnuclear star forming ring and it is marked (with a dashed circle) in the images and spectral maps from the MEGARA cube, as well as, in the *HST* image in the middle panel of Fig. 1.

We checked the wavelength calibration and obtained the instrumental profile using two OH sky-lines (λ6499 and λ6554) bluewards to H α-[N II]; sky-lines are absent in the red part of the spectra. The mean central wavelengths were found to be 6498.725 ± 0.046 Å and 6553.621 ± 0.047 Å coinciding well with their actual values i.e. 6498.729 and 6553.617 Å from Osterbrock et al. (1996). The width (σ) of the two sky-lines (instrumental dispersion) is uniform over the entire field of view with average and standard deviation values of 0.12 ± 0.05 and 0.14 ± 0.05 Å. The results of these checks indicate negligible systematic calibration errors and will affect our measurements of the ionized gas kinematics (Section 3). Hence, hereafter, the fitting errors (generally larger than 0.1 Å) would be considered as the main source of uncertainty.

For each spectrum (i.e. on spaxel-by-spaxel basis), the effect of instrumental dispersion (σ_{INS}) was corrected for by subtracting it in quadrature from the observed line dispersion (σ_{obs}) i.e. $\sigma_{line} = \sqrt{\sigma^2_{obs} - \sigma^2_{INS}}$.

The field of view of MEGARA observations is overlaid to the *HST*-WFPC2 (Wide-Field Planetary Camera 2) image shown in the left-hand panel of Fig. 1. In order to highlight features departing from axisymmetry, we produced the 'sharp-divided' image (Fig. 1, middle). It is obtained by dividing the original image, *I*, by a filtered version of it (Márquez et al. 1999, 2003). The image is median filtered with the IRAF[4] command 'median' using a box of 20 pixels.

The right-hand panel of Fig. 1, shows the optical continuum (6380–6480 Å, rest frame wavelength range) image generated from the MEGARA-IFU datacube. Throughout the paper, we consider the peak of the continuum emission as the photometric centre (nucleus) of the galaxy with an accuracy of 0.47 arcsec (half of the FWHM of the PSF). It is marked as a cross in all images and spectral maps obtained from the MEGARA cube.

3 EMISSION LINES MODELLING AND MAPS GENERATION

All the spectra in the cube were visually inspected in order to check and correct for possible data reduction artefacts (e.g. residual comics rays), as well as to look for the presence of line asymmetries and complex line profiles. These latter are present at nearly any distance from the nucleus. Moreover, most of the spectra in the unresolved nuclear region of NGC 7469 (at $r \leq 1.85$ arcsec, i.e. ∼630 pc at the

[1] https://github.com/guaix-ucm/megaradrp/
[2] https://doi.org/10.5281/zenodo.1974954

[3] Hereafter, as 'spaxels', we will refer to all the spatial elements (pixel) in the cube obtained after the application of the regularization grid (not those from the fully reduced RSS cube).
[4] http://iraf.noao.edu

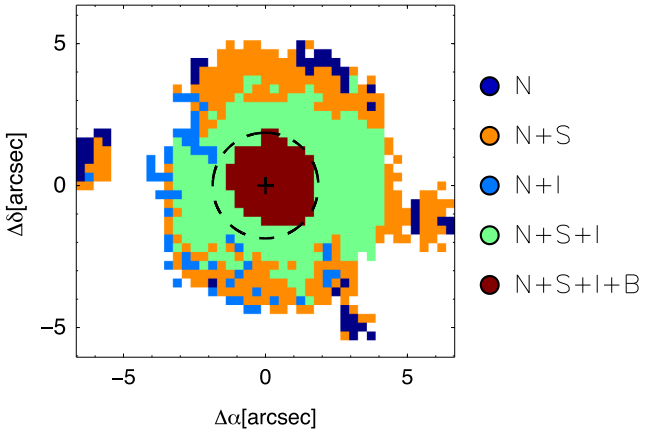

Figure 2. Map of the number of components used to model the observed line profiles in the MEGARA cube (Section 3.1). The colour coding indicates the different combinations of components considered for the final fits. These are indicated in the legend where 'N','S', 'I', and 'B' stand for narrow, second, intermediate-width, and broad components, respectively. For each of the five possible combinations of components, examples of the fits are shown in Fig. 3.

adopted distance, see Table 1), show broad H α λ6563 emission line superposed with strong narrow lines, which is typical for a Seyfert 1 nucleus.

We excluded from the fitting procedure those spectra with signal-to-noise per pixel (SNR) in H α lower than 15 and those with artefacts. These are the 57 per cent of the total number of spaxels.

This conservative limit in SNR will allow us to maximize the exploitation of the unprecedent spectral resolution of MEGARA data.

We did not apply any procedure for the subtraction of the underlying stellar light for MEGARA spectra as their wavelength coverage (Section 2) prevents an optimal stellar-continuum modelling.

3.1 Line fitting

The H α and [N II] $\lambda\lambda$6548,6584 emission lines were simultaneously modelled with Gaussian functions using a Levenberg–Marquardt least-squares fitting routine (MPFITEXPR) by Markwardt (2009), within the Interactive Data Analysis[5] (IDL) environment. We tied all the lines to have the same line-width and velocity shift. We imposed also that the intensity ratio between the [N II] λ6548 and the [N II] λ6584 lines, satisfies the 1:3 relation (Osterbrock & Ferland 2006).

The procedure for fitting H α-[N II] takes into account possible multiple line components. Specifically, we realized that four distinct kinematic components (two narrows, one broad, and one of intermediate width) were sufficient. This number of components ensures a trade-off between the kinematical details, the SNR, and the goodness of the fit (see Bosch et al. 2019). Specifically, four components represent the largest meaningful number of components to perform the kinematics analysis throughout the galaxy. Fig. 2 shows a map of the number/combinations of the components used during the line-fitting procedure. Fig. 3 shows examples of the Gaussian fits.

The procedure is organized in different steps and is aimed at obtaining the best-fitting to the H α-[N II] emission features.

To prevent overfit models and identify possible broad wings or double peaks, we cannot rely on the chi-square (χ^2) estimator as the

[5]http://www.harrisgeospatial.com/SoftwareTechnology/IDL.aspx

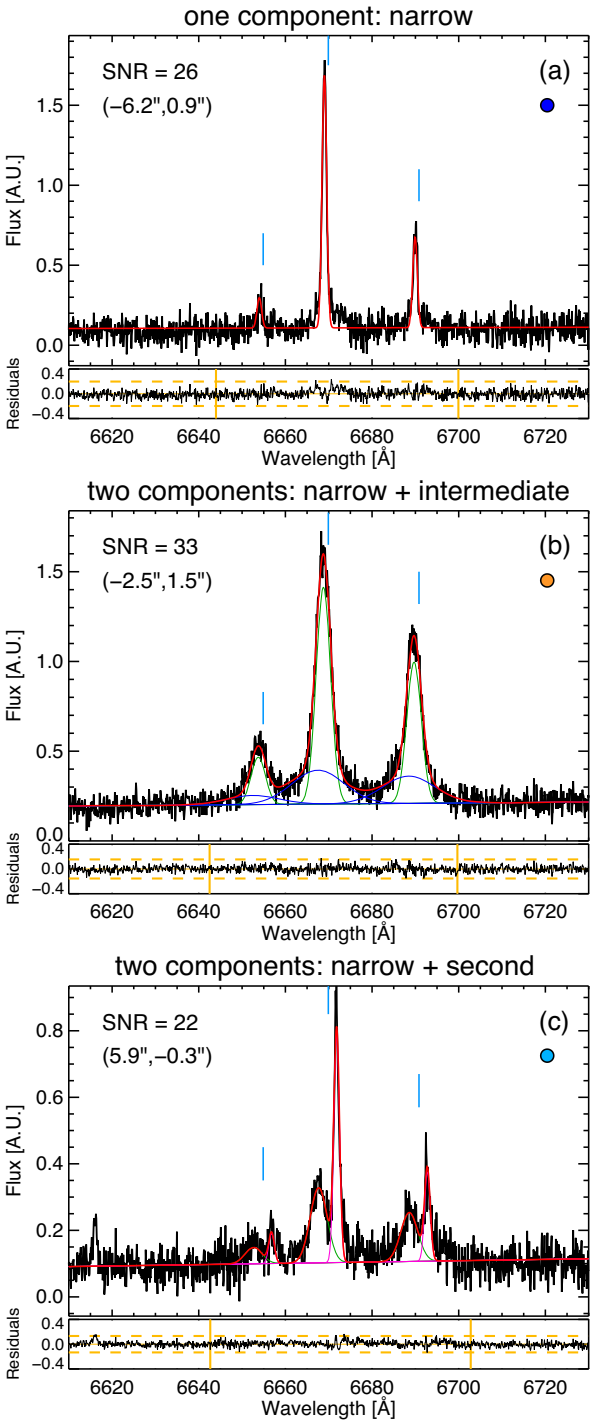

Figure 3. Examples of H α-[N II] observed spectra and their modelling for selected regions. The coordinate labels indicate distance from the photometric centre (Section 2). As reference, blue vertical lines mark the systemic wavelengths of the emission lines. For each spaxel (from 'A' to 'E' panels) the modelled line profile (red continuous line) and the components (with different colours) are shown. Specifically, green, pink, blue Gaussian curves indicate: narrow, second, and intermediate components used to model [N II] lines and narrow H α; in purple is marked the broad H α component from the BLR (see Section 3.1). Same colours mark the same components that are summarized at the top. Small circles follow the colour coding of Fig. 2. Residuals from the fit (i.e. data model) are in the small lower panels in which orange dashed lines indicate the $\pm 3\times \varepsilon_c$. Vertical orange continuous lines mark the wavelength range considered for calculating $\varepsilon_{\rm line}$ for the different cases (Section 3.1).

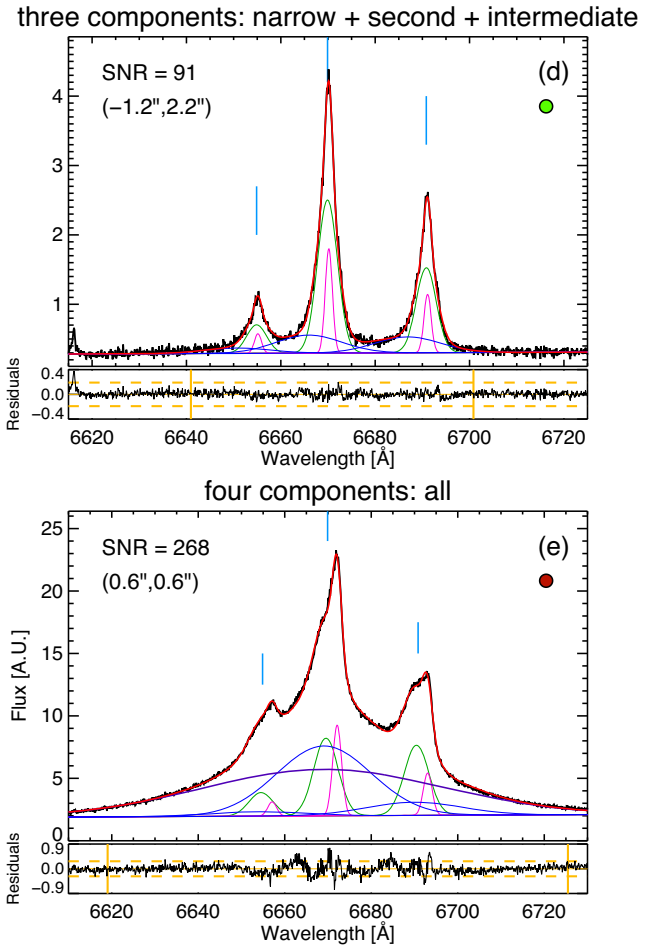

Figure 3 – *continued*

goodness of the least-square minimization depends to the number of components (Bosch et al. 2019). Therefore, to allow for the appropriate number of Gaussians, we followed the method proposed by Cazzoli et al. (2018) and already successfully applied to optical spectra of active galaxies (see also Cazzoli et al. 2018, Hernández-García et al. 2019 and Hermosa-Muñoz et al. 2020), on a spaxel-by-spaxel basis. More specifically, to assess whether the addition of a component is significant, we first calculated the standard deviation of a portion of the continuum (30 Å) free of emission lines, i.e. ε_c. Then, throughout all the steps of the line fitting procedure (from one to four components), we compared the ε_c value with the standard deviation estimated from the residuals under Hα-[N II], i.e. ε_{line}, in a wavelength range[6] of $\sim$60 Å ($\sim$100 Å if the broad component is included in the fitting). We considered a reliable fit with an adequate number of components when $\varepsilon_{line} < 3 \times \varepsilon_c$ (a '3-σ significance' criterion), otherwise we tested the inclusion of an additional component. Finally, we also checked the results from the fits by visually inspecting all the residuals before and after the addition of a component.

The procedure is organized as follows. Initially, we fit all the emission lines to a single component, i.e. one Gaussian per each [N II] line and narrow Hα (hereafter, narrow component, Fig. 3 A).

[6]The wavelength ranges were selected in order to cover the Hα-[N II] complex and taking into account possible blue/red-shifted components.

In those cases where the observed line profiles show asymmetries (broad wings), the procedure adds a second Gaussian component of intermediate width (hereafter, intermediate component, Fig. 3 B). The two-Gaussian fits lead to two components which in general can be distinguished according to their widths i.e. narrow ($\sigma \leq 3$ Å, mostly) and intermediate ($\sigma \geq 4.5$ Å, generally) components. Then, we add a third Hα component originated in the broad-line region (BLR) of the AGN (hereafter, broad component), in most of the spectra within the nuclear region (see Section 2). This component can be clearly distinguished from the other two previously considered as the typical line width is larger than 17 Å (i.e. more than 40 Å in FWHM). Some of the spectra have double-peaked and/or asymmetrical profiles (e.g. Figs 3 C and D) that suggest the presence of an additional narrow component (i.e. with a width lower than the intermediate-component). Therefore, for these spectra we used three components (including the intermediate one) for the fit of [N II] lines and narrow Hα (Fig. 3 E). In some cases, although the second component seemed necessary, the modelling of the Hα-[N II] lines was rather complicated leading to residuals with substructures. Therefore, in those circumstances, in order to reproduce well the line profiles, the second component was constrained to have a width lower than 3.5 Å. These limits allow us to constrain the overall procedure to deliver meaningful results lowering the residuals (measured in terms of $\varepsilon_{FIT} = \varepsilon_{line}/\varepsilon_c$).

Overall, the final line modelling was satisfactory. The procedure reproduces well the observed line profiles with low residuals (see lower panels in Fig. 3). The few exceptions to this general behaviour are seen in the central region (i.e. within the region affected by the PSF marked as dashed circle in all maps, see Section 2), where although residuals are within the significance of $\pm 3\times\ \varepsilon_c$ some substructures seem to exist (e.g. Fig. 3 E). These features might indicate that a Gaussian-fit to the broad BLR-emission is a simplification (e.g. Lorentzian profiles, see Kollatschny & Zetzl 2013 and references therein). A detailed modelling of the (unresolved) BLR-emission is beyond the aim of the paper.

In general, the final values for ε_{FIT} are never larger than 3, being larger than 2 only in 6 per cent of the cases (46 out of 738 total spaxels considered); on average ε_{FIT} is 1.2.

As a further check, in few representative example of the fit well outside the nuclear region (see Fig. 3), we verified if the number of the selected Gaussian components (N) is adequate, i.e. all statistically significant and there is no need of increasing the number of components. This test was done using the Akaike Information Criterion indicator (AIC; Akaike 1974) which enable the comparison of models with different number of components (see Bosch et al. 2019). In all the cases, the number of components is very strong justified by a Δ AIC defined as: AIC_{N+1} - AIC_N, larger than 10 (Wei, Wu & Melia 2016).

Formal fitting errors are the 1-sigma parameter uncertainties weighted with the square-root of the reduced χ^2 (see MPFITEXPR documentation). These are larger than calibrations errors (see Section 2 for the latter) on average, i.e. (0.2 versus 0.12) Å and (0.1 versus 0.05) Å for central wavelengths and widths, respectively.

3.2 Generation of spectral maps

From the MEGARA datacube, we generate the continuum image which is shown in Fig. 1 as reference and in comparison to *HST* images.

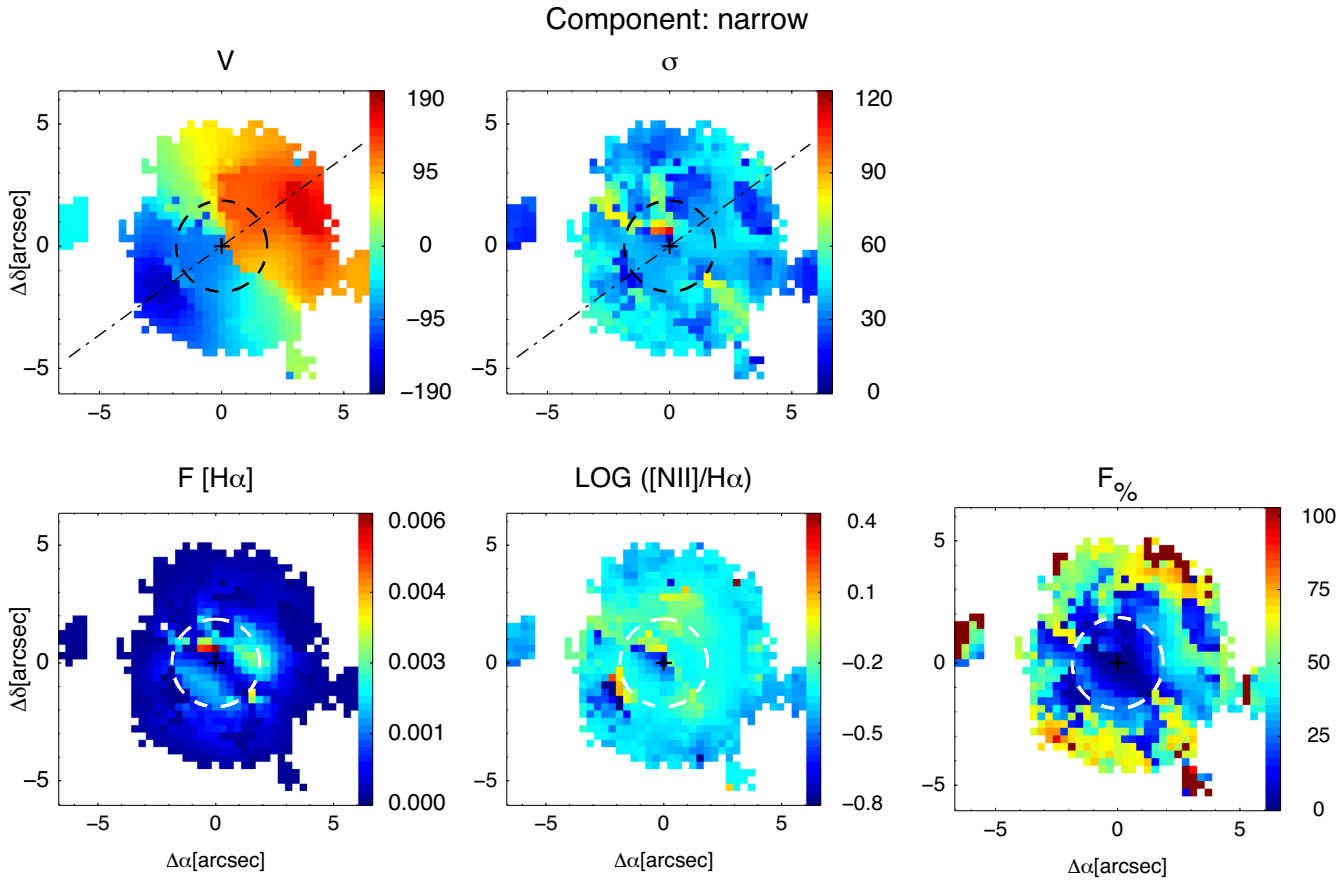

Figure 4. Ionized gas maps derived from the fit to the H α-[N II] emission line profiles for the narrow component. *Top panels*: kinematic maps, i.e. the velocity field (V) and the velocity dispersion map (σ). These are in km s^{-1} units and they are colour coded according to their own scale (i.e. range of the velocity and velocity dispersion) to facilitate the contrast and to highlight weak features. *Bottom panels*: from left to right, H α flux-intensity map (F[H α]), [N II]/H α line ratio and that of the percentage contribution of the narrow component to the total H α-[N II] emission ($F_{\text{per cent}}$). The former is in arbitrary units as no flux-calibration has been applied (Section 2). The latter is shown with the 0 – 100 per cent range to enable the comparison with the same kind of map but for different components (Figs 5 and 6 bottom right). The cross marks the photometric centre, the dashed circle indicates the nuclear region (Section 2). The dot-dashed line is the major photometric axis oriented accordingly to photometric PA (Table 1).

For each emission line and component found with the procedure described in Section 3.1, we end up with the following information: central wavelength, width, and flux intensity along with their respective fitting errors. The intrinsic line widths were computed after removing the instrumental profile inferred from the sky lines (Section 2).

Whereas the narrow and second components have a similar range of central wavelengths,[7] a clear distinction in line width exists, reaching up to a factor of 10 (on average was ∼3). Hence, by first generating the map of the ratio between the widths of the two components, we were able to differentiate the two narrow components. i.e. systemic (or narrow) and second (broader) components, according to their widths, and then map their properties (fluxes and velocities and the corresponding errors). Note that, the ranges of values for the velocity dispersion of these two narrow components partially overlap. However, the overlap is not uniform within the entire IFU field varying spatially. Therefore we cannot fix line widths of the narrow components and a spaxel-by-spaxel basis is appropriate. For intermediate and broad component a clear difference in width already exists after the line fitting is applied procedure as mentioned in Section 3.1.

By means of in house IDL procedures, we generate maps of: flux intensity, velocity field (V), and velocity dispersion (σ), for all the four components. The kinematics maps (velocity and velocity dispersion) are displayed in Figs 4–6 along with those for the H α flux intensity (F [H α]) and the percentage contribution ($F_{\text{per cent}}$) of each component to the total H α-[N II] emission. For each component used to model [N II] lines and narrow H α, the maps of the ratio between [N II] λ6584/H α were also generated. The histograms of the distribution of the line ratios are presented in Fig. 7.

The radial velocity maps are scaled to the systemic velocity defined as $c \times z$, i.e. 4891.7 km s^{-1} (z is the redshift, Table 1). The observed systemic radial velocity is 4839.9 (4800.2) km s^{-1} being measured as the velocity of the narrow (second) component at the brightest spaxel in the continuum image. This spaxel is marked with a cross in all the maps from the MEGARA datacube which we assume to be the nucleus of the galaxy (photometric centre). The velocities measured at the position of the photometric centre are similar (within less than 2 per cent) to the assumed systemic velocity ($c \times z$).

[7]Differences in the velocities of the two narrow components are of about 0.9 Å, i.e. ∼40 km s^{-1}, on average. This value should not be considered as a systemic offset since the difference in velocity varies throughout the MEGARA IFU field (Sections 5.1 and 5.2; Figs 4, 5, and 8).

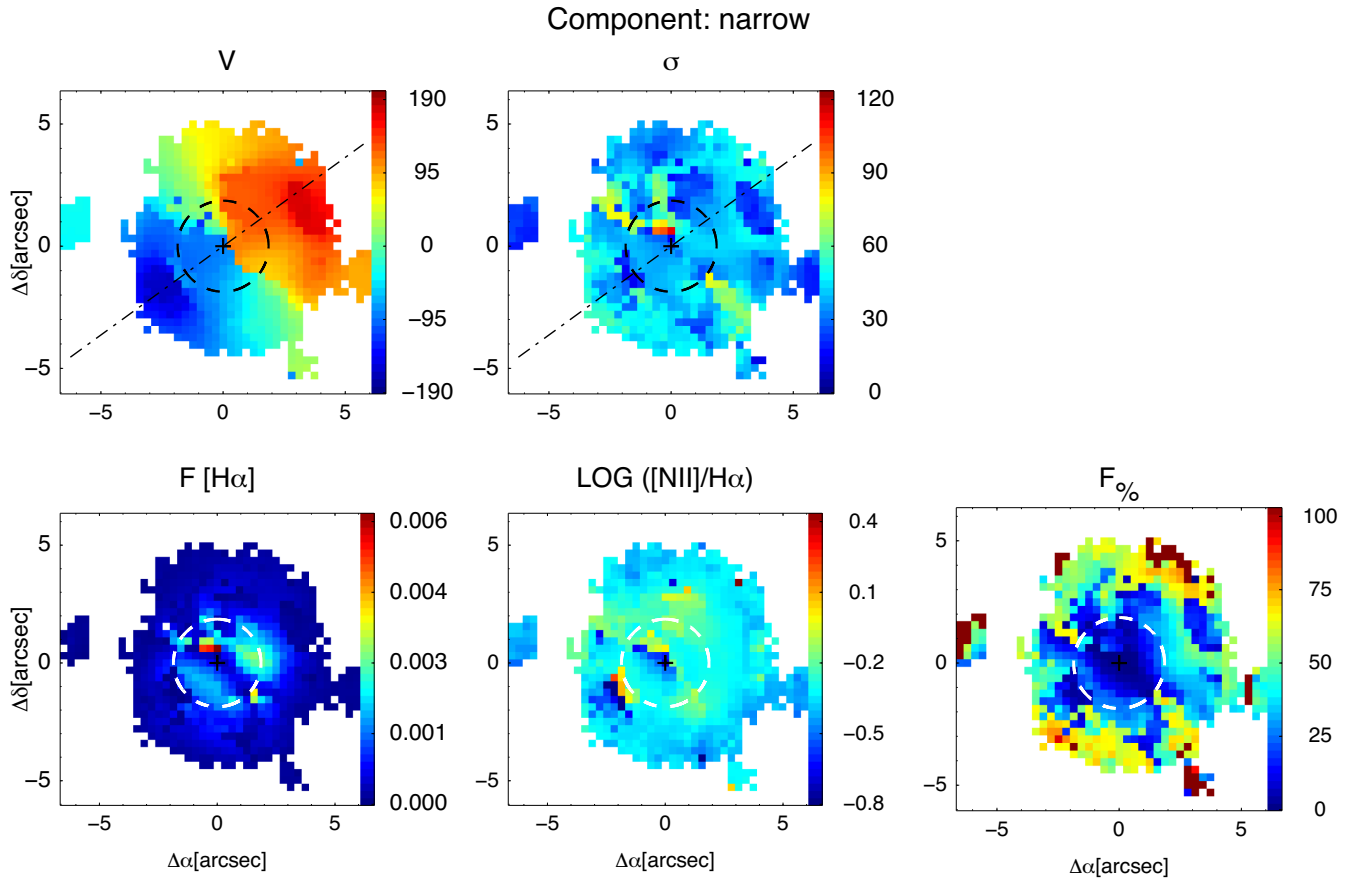

Figure 5. The same as Fig. 4, but for the second component.

Velocities are barycentric, we did not apply any correction for the heliocentric velocity which is of 21.4 km s^{-1} as determined with the IRAF command 'rvcorrect'.

All the maps are displayed using the plotting package JMAPLOT by Maíz-Apellániz (2004).

4 KINEMATIC ANALYSIS

4.1 Position velocity diagrams

As we will discuss in Sections 5 and 6, the kinematics of both narrow and second component show signatures of a rotating disc. Therefore, from the kinematic maps of both components (Figs 4 and 5, top panels) we extracted the velocity values in a 0.6 arcsec pseudo slit along their major kinematic axis. To obtain the corresponding position–velocity diagrams ('PV diagrams'), shown in top panels of Fig. 8, we rescaled the velocities to the kinematic centre. It is defined, for each component, as the velocity for which the rotation curve, Fig. 8 bottom panels, is symmetric. For the narrow (second) component the velocity of the kinematic centre is 4895.7 km s^{-1} (4874.2 km s^{-1}) and it is located within 0.15 arcsec (0.8 arcsec) from the photometric centre. The PV curves for narrow and second components show distinct shapes (Sections 5.1 and 5.2) which will be discussed in detail in Section 6.2. At the same locations of the PV curves, we extracted the corresponding velocity dispersion measurements. These will be discussed in comparison with the results of our disc modelling in Section 4.2.

4.2 Disc modelling with KINEMETRY

To obtain a physically meaningful fit to the observed velocity field and velocity dispersion maps, and to robustly identify and quantify the possible deviations from an ideal rotating disc, we applied the KINEMETRY package (version 4.2) developed by Krajnović et al. (2006) and methodology. Briefly, this procedure is an extension of surface photometry to the higher order moments of the velocity distribution. More specifically, the KINEMETRY algorithm describes the data by a series of concentric ellipses of increasing major axis length. Along each ellipse, the moment as a function of angle is then extracted and decomposed into the Fourier series following the *cosine*-law approximation (i.e. the velocity field in an ideal rotating disc is expected to be dominated by the *cos*-term; Shapiro et al. 2008).

The disc-kinematic modelling and the extraction of the kinemetric parameters is done with KINEMETRY as follows. The first step is to locate the centre of the system, around which the ellipses are constructed. We assumed that the kinematic centre is coincident with the photometric centre (i.e. the peak of the continuum emission, Section 3.2). Other relevant geometric parameters (i.e. position angle and inclination) will be derived during the KINEMETRY analysis at each ellipses's position (in steps of 0.31 arcsec). Then, as the high SNR emission has an irregular morphology and it is not covering all the FoV (Section 3), we relax the condition in the keyword 'COVER' which controls the radius at which the extraction of values from maps stops. We considered the value of 0.60 (default is 0.75) meaning that if less than the 60 per cent of the points along an ellipse are not present the procedure is interrupted. With these

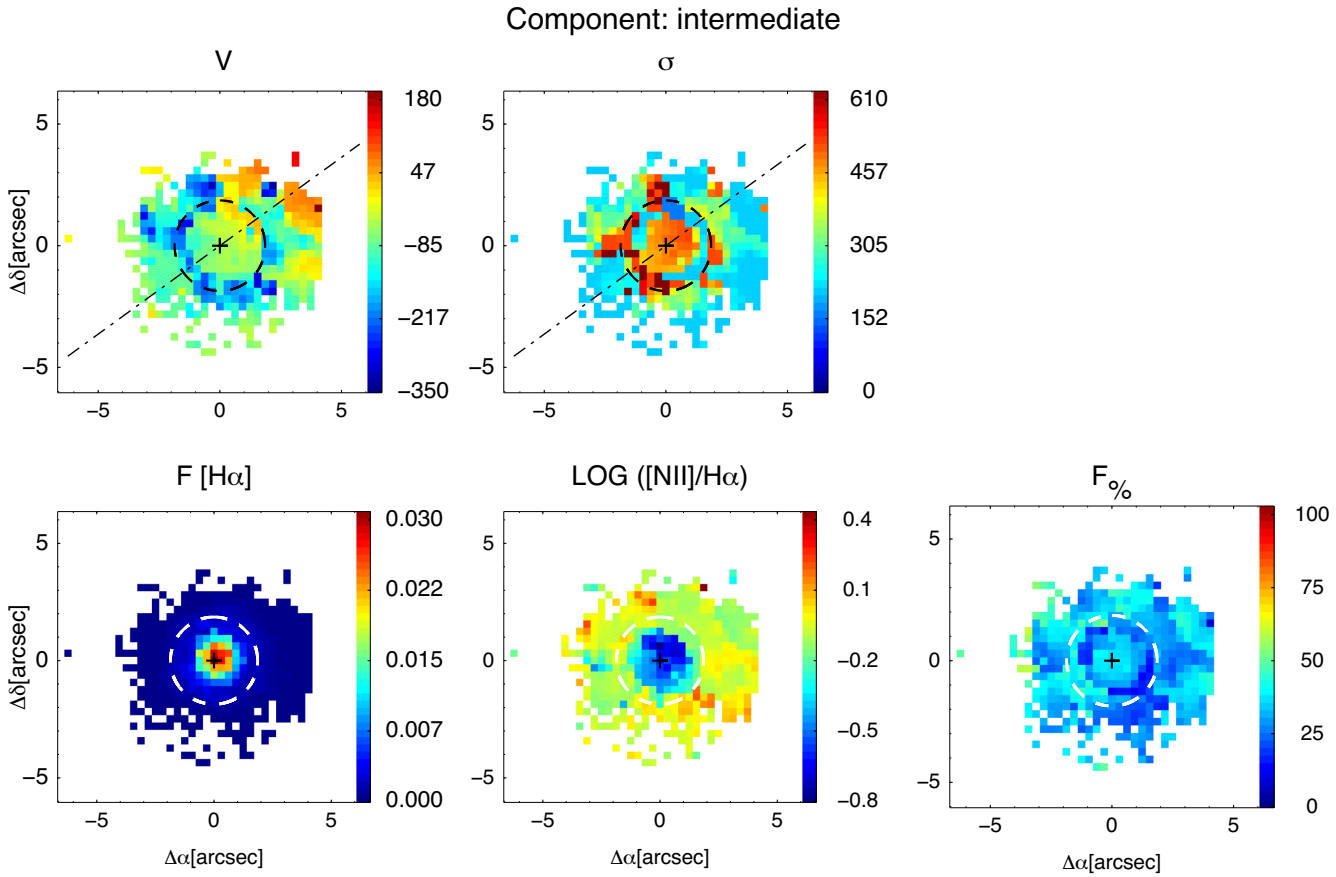

Figure 6. The same as Fig. 4, but for the intermediate component.

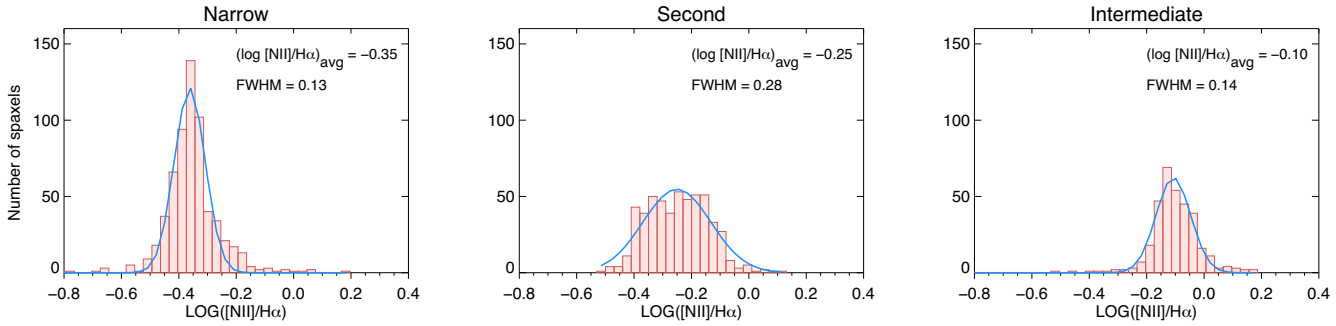

Figure 7. Distribution of the logarithm of the [N II]/H α line ratio for the three components (indicated at the top of each panel) used to model [N II] lines and narrow H α during this work (Section 3.1). We only considered the measurements outside the nuclear region (dashed circle in all spectral maps). As reference, in all panels, the Gaussian fit to the distribution of the values for the wavelength and width is marked with a continuous blue line. Average values and the FWHM of the Gaussian fit are reported on the top right. All histograms are binned in 0.03 dex-wide.

prescriptions, we generated the model map for the velocity field of the narrow component. This is shown in Fig. 9 (upper panels) where we show the observed and reconstructed maps as well as the residuals. In Fig. 10 the selected kinemetric coefficients relevant for the characterization of the disc kinematics are displayed as a function of the distance from the centre of the system. These coefficients are 'Γ': the kinematic PA; and 'q': the flattening of the fitting-ellipse. Then for the velocity: 'k_1'measures the amplitude of bulk motions (rotation curve) and 'k_5' the deviations from a rotation disc pattern. The kinematic PA has been also obtained independently ($\Gamma_{\rm FIT}$) using the method described in Appendix C of Krajnović et al. (2006) via the IDL routine FIT_KINEMATIC_PA (see also Cappellari et al. 2007).

As the velocity dispersion map of the narrow component deviates from what is expected in the case of an ideal rotating disc (see Section 5.1), we consider to use KINEMETRY with an additional constraint. Specifically, the velocity dispersion map is reconstructed along the best-fitting ellipses from the modelling of the velocity field of the narrow component. The model map, the reconstructed map, and the residuals are shown in Fig. 9 (lower panels). For velocity dispersion, the kinemetric coefficients considered are: 'A_0', the velocity dispersion profile with radius and 'B_4', the shape parameter

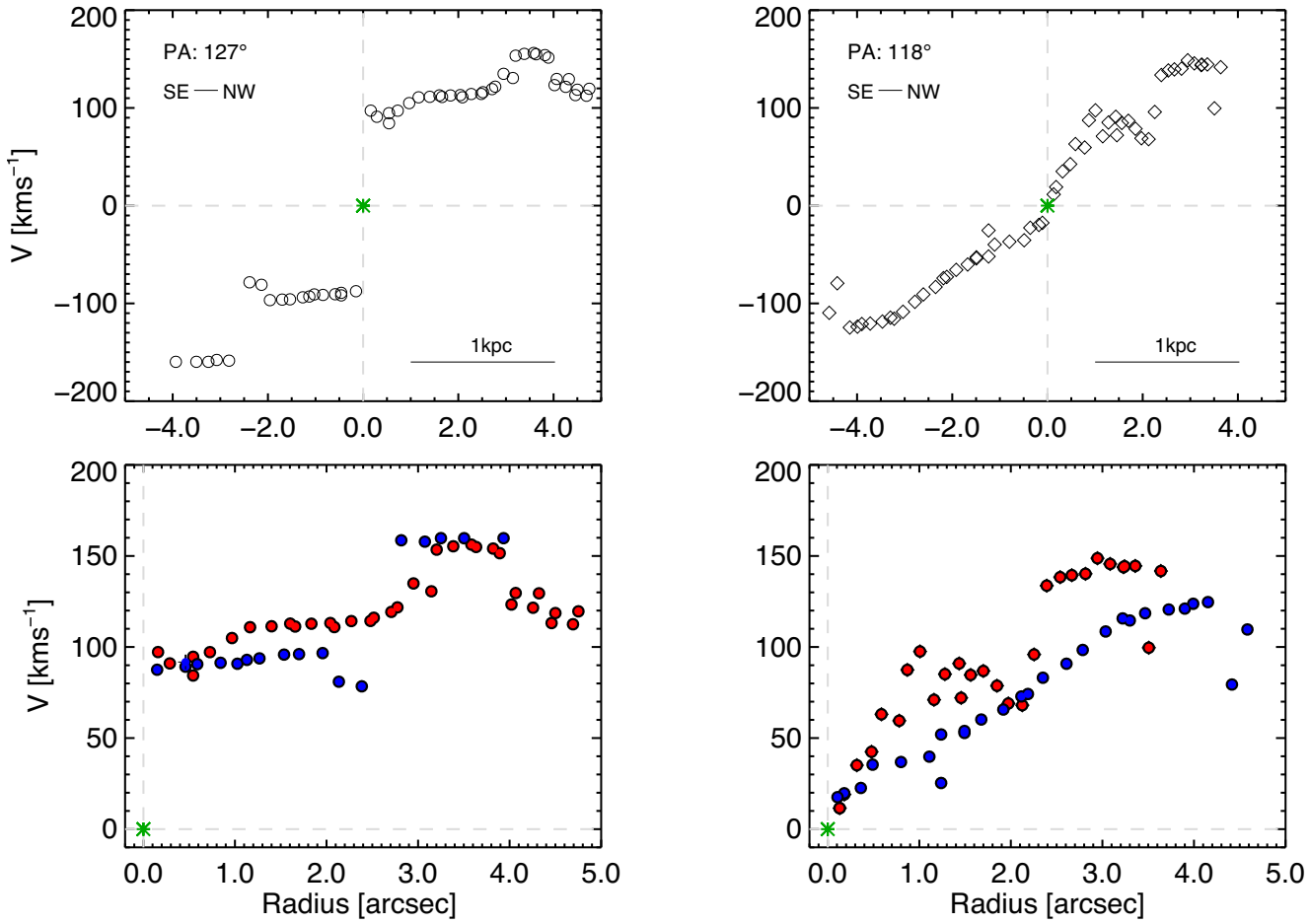

Figure 8. PV and rotation curves for the narrow (left-hand panel) and the second (right-hand panel) kinematic components, upper and lower panels, respectively. PV curves were obtained considering a pseudo-slit aligned according to the major axis of their rotation. The circles and diamonds indicate the point for the narrow and second kinematic components, respectively. The radius is calculated as the distance from the kinematic centre that is marked with a green asterisk (see Section 4.1). In the bottom panels, blue and red symbols indicate the approaching (negative velocities) and receding sides (positive velocities) of the rotation, respectively. In all panels, grey dashed lines show zero-points for position and velocity, as reference. The typical uncertainty on the velocity measurements is generally $\leq 8\,\mathrm{km\,s^{-1}}$. Hence, error bars are not showed as being comparable with the symbols size.

(see Fig. 10). The latter is used to quantify anisotropies, being the analogous of the photometric term that describes the deviation of the isophotes from an ellipse (Krajnović et al. 2006). Specifically, negative values are indicative of boxiness (triaxal structure, slow rotation), while positive values of disciness (oblate, fast rotators), see e.g. Emsellem et al. (2007) for further details.

The velocity dispersion map of the narrow component (Fig. 4 top right) shows an enhancement along the minor axis (green colours, $\sigma \geq 60\,\mathrm{km\,s^{-1}}$) as well as a decrement in a few peculiar regions of the IFU field (blue colours). These sub-structures possibly perturb the disc kinematics, as we comment in Section 5.1 and discuss in Section 6.4.

In order to test if the results from KINEMETRY are influenced by these features, we also executed KINEMETRY for the velocity dispersion map of the narrow component masking them out. Specifically, we first build a mask flagging individual spaxels in the velocity dispersion map of the narrow component at the location of all substructures. Then we combined it, within KINEMETRY, with the same set of parameters as in the previous disc-modelling. The results of this test will be discussed in Sections 5.1 and 6.2 (see also Fig. 10, orange circles).

The estimation of the dynamical ratio and scale height (V/σ and h_z, respectively), defined and discussed in Section 6.3, for the second narrow component suggest the presence of a dynamically hotter and thicker disc. Therefore, we did not attempt to model with KINEMETRY (suited for thin discs) the velocity and velocity dispersion maps of the second component.

In Fig. 11 (upper panel), the rotation curve from KINEMETRY is compared to that from the symmetrization of the PV curve (Fig. 8 bottom left) and those from previous works. Similarly, the velocity dispersion radial profile obtained from KINEMETRY (Fig. 10 green circles) and from the MEGARA map (obtained as the PV measurements, Section 4.1) are displayed (middle panel). We also show the dynamical ratio calculated along each ellipse (bottom panel; see discussion in Section 6.3).

5 MAIN OBSERVATIONAL RESULTS

In Table 2, we summarize the kinematic parameters and characteristic values of the [N II]/Hα ratio and the contribution of the four components considered in this paper (Section 3.1).

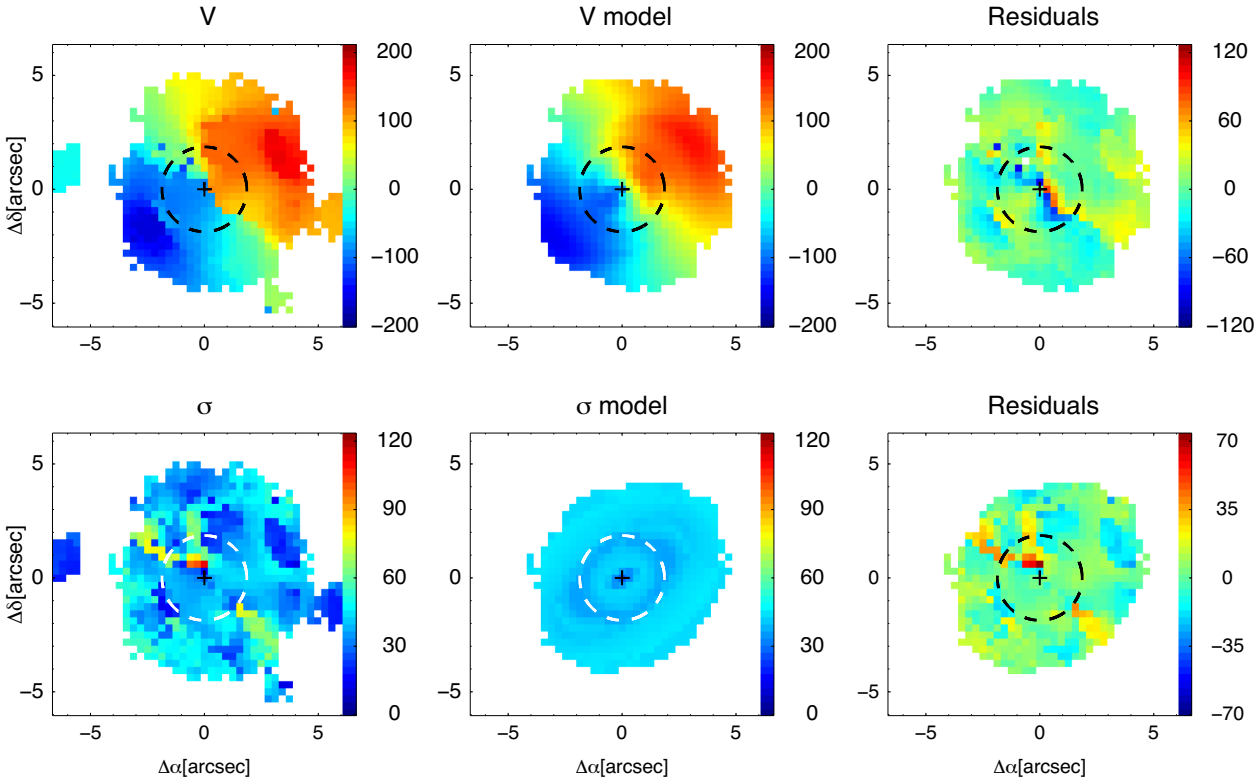

Figure 9. For the narrow component, the maps of the Hα velocities (top) and velocity dispersion (bottom) and their respective reconstructed (middle) and residual (data model, right) maps for NGC 7469 (se also Section 4.2). The cross marks the photometric centre and the dashed circles indicates the nuclear region (Section 2). All the maps are in km s^{-1} units.

5.1 Narrow (systemic) component

The maps of the ionized gas kinematics as traced by the Hα-[N II] lines (narrow component) are shown in Fig. 4 (top panels). The velocity field (Fig. 4, top left) presents a point-antisymmetric velocity pattern consistent with large kiloparsec-scale ordered rotational motions (e.g. a rotating disc). The peak-to-peak semi-amplitude of the velocity field is 163 ± 1 km s^{-1} (ΔV, Table 2), with the maximum velocity gradient oriented in the southeast–northwest direction with a position angle $PA_{maps} = (125 \pm 10)^{\circ}$ (Table 2). This value is in remarkably good agreement with the PA of the photometric major axis (PA_{phot}) from Hyperleda, i.e. 126° (Table 1).

The velocity dispersion map (Fig. 4, top right) shows an irregular pattern and it is not centrally peaked, contrary to what is expected for a rotating disc. The maximum value of the velocity dispersion map (108 ± 4 km s^{-1}) is in fair positional agreement (within 0.6 arcsec, i.e. 200 pc) with the nucleus. The average velocity dispersion inside the nuclear region (i.e. σ_c, 40 ± 1 km s^{-1}, Table 2) is rather similar to that in the putative disc (i.e. σ_{avg}, 38 ± 1 km s^{-1}, Table 2). In this comparison, it has to be noted that there are some irregularities. Specifically, there are eight regions (six in the main disc and two at $r > 5.0$ arcsec) of low velocity dispersion (i.e. $\sigma < 30$ km s^{-1}). Furthermore, the velocity dispersion is enhanced (typically $\sigma > 60$ km s^{-1}) along the minor axis of the putative disc rotation towards north-east and south-west direction, up to $r \sim 3.7$ arcsec. All the anomalies of the velocity dispersion maps will be discussed in Section 6.4. These features are identified in the maps shown in Fig. 12.

For the narrow component, the regular pattern of the velocity map (Fig. 4, top left) indicates a relatively undisturbed velocity field without any strong signature of non-circular motions. The corresponding PV curve is nearly symmetric (Fig. 8 top left). It seems to level out at ~ 150 km s^{-1}, after a well-resolved and steep rise in the receding side (positive velocities) in the north-west direction. The approaching side (negative velocities, to the south-east) is slightly more irregular showing a discontinuous rise.

The models produced with KINEMETRY (Section 4.2) satisfactorily reproduce the data, in particular, for the velocity (Fig. 9 top). Indeed, for the majority of the spaxels (i.e. 63 per cent) in the residual map, data model (Fig. 9 top right), the values are lower than 15 km s^{-1}. Larger negative residuals (> 50 km s^{-1}) are seen in correspondence of the minor axis of the rotation.

The reconstructed velocity dispersion map is not centrally peaked showing one 'drop' of ~ 25 km s^{-1} (Fig. 9 bottom). This feature is observed at $r \leq 1.5$ arcsec. It is distinctly visible in the velocity dispersion radial profile in Fig. 10 (right) either when including (green circles) or excluding (orange circles) possible velocity dispersion substructures (see Section 4.2). Such a velocity dispersion decrement is possibly related to a σ-drop (the velocity dispersion is depressed in the galaxy centre) as discussed in Section 6.2.

When comparing the results from the KINEMETRY modelling including/excluding possible velocity dispersion anomalies some variations are seen for the B_4 parameter. In the majority of the cases (8 out of 13 measurements) the shape of the ellipses is preserved (either discy or boxy) being the B_4/A_0 ratio the same within uncertainties in half of these cases (4 out of 8). For the other five cases, the B_4/A_0 ratios have different signs indicating either the disciness or boxiness of the ellipses (Fig. 10 bottom-right). The instability of the B_4 term could be due to the limitation of the parameters space for KINEMETRY, e.g. for a given input ellipse, since the number of points is lower due to the masking.

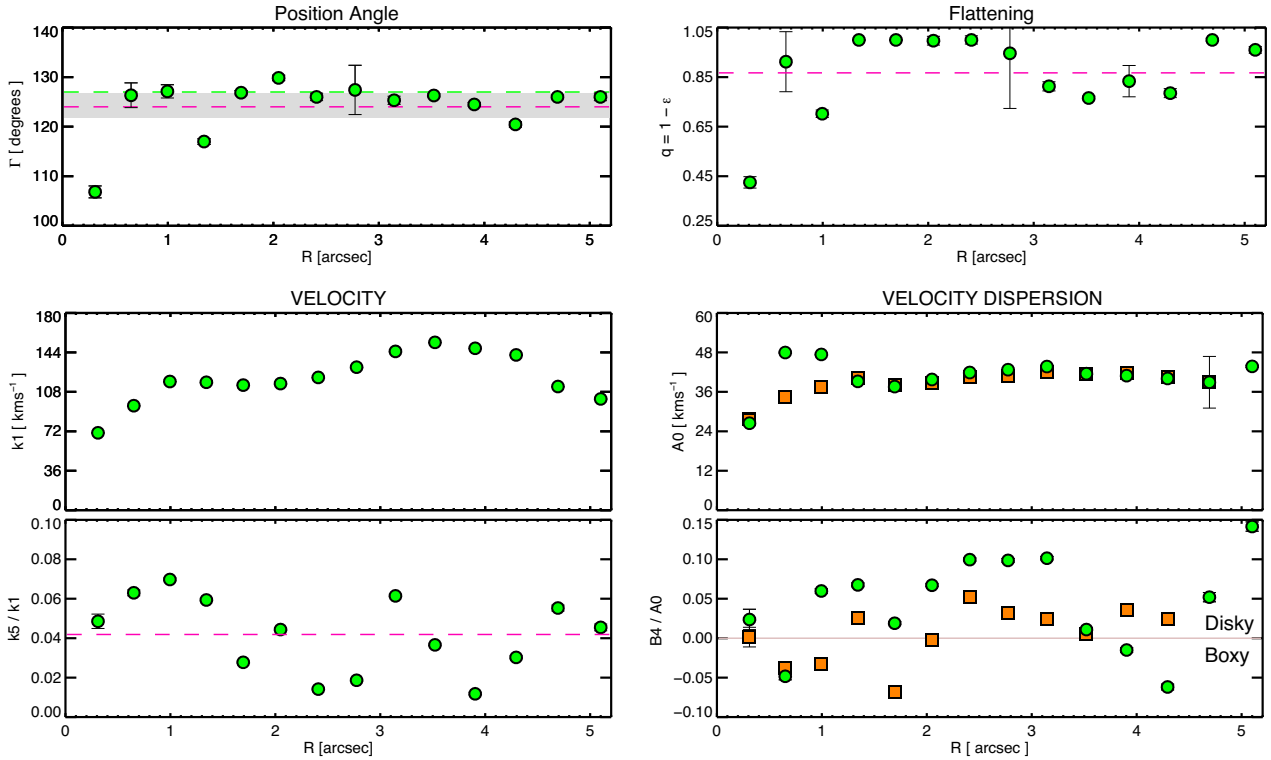

Figure 10. Green circles mark the radial profiles of the kinemetric parameters describing the model in Fig. 9. In the upper panels, the position angle Γ and the flattening q of the best-fitting ellipses (ε is the ellipticity) are shown. In the lower panels, on the left, we display the first (k_1) and fifth order (k_5) of the Fourier terms, as well as, on the right, the intensity and shape parameter (A_0 and B_4, respectively). In the top left-hand panel, magenta and green dashed lines indicate the average values of Γ and $\mathrm{PA}_{\mathrm{maps}}$ (i.e. the major axis of the rotation from observed maps, Fig. 4, Table 2) respectively. In grey, the range of values for $\Gamma_{\mathrm{FIT}} = (124.3 \pm 2.5)^{\circ}$ resulting from the method for calculating the PA by Krajnović et al. (2006) (see Section 4.2). The value for the photometric PA, $\mathrm{PA}_{\mathrm{phot}}$ (Table 1), is not marked but is in good agreement with the value of $\mathrm{PA}_{\mathrm{maps}}$ (Table 2). In the bottom left-hand panel, the dashed magenta line marks the average value of k_5/k_1 (~ 0.04; see Krajnović et al. 2011). In the bottom right-hand panel, the light pink line indicates the zero, which is also the dividing line indicating the deviations of the iso-σ contours from an ellipse, i.e. boxiness and disciness (negative and positive values, respectively; Krajnović et al. 2006). The orange squares mark the radial profiles of the kinemetric parameters from the test described in Section 4.2 for which we excluded all the anomalies in the velocity dispersion map (Sections 5.1 and 6.4). Note that, due to this masking, KINEMETRY halts at $r \sim 4.8$ arcsec. In all panels, uncertainties are the formal ($1\,\sigma$) errors of the coefficients which are returned by KINEMETRY.

From this comparison, we excluded the values at $r > 4.8$ arcsec as, when velocity dispersion anomalies are masked out, at this radius KINEMETRY halts (see Section 4.2).

The position angle from KINEMETRY, Γ, is remarkably stable with values within 120° and 130° over the most of the sampled radius (with only 3 exceptions, Fig. 10 top left). The average value of Γ ($\sim 125^{\circ}$) is consistent with those obtained with different estimates, i.e. from a direct estimate using the observed maps $\mathrm{PA}_{\mathrm{maps}} = (125 \pm 10)^{\circ}$, Table 2) and from the output of the FIT_KINEMATIC_PA routine (Section 4.2), i.e. $\Gamma_{\mathrm{FIT}} = (124.3 \pm 2.5)^{\circ}$.

The q parameter has values between 0.4 and 1 (Fig. 10 top right). The average (median) value of q is 0.88 (0.94), indicating that the modelled velocity map for the narrow component is kinematically round. In the special case of a disc where the motions are confined to the plane (thin-disc approximation, see also Section 6.3) the flattening is directly related to the inclination of the disc, i.e. $q = \cos(i)$ (Krajnović et al. 2006). This would imply an inclination of 31.5°, that is consistent within 1 per cent with the value reported in Hyperleda (i.e. 30.2°, Table 1).

The map of the Hα flux-intensity (F[Hα]) and that of the percentage contribution to the total Hα-[N II] emission ($\mathrm{F}_{\mathrm{per\ cent}}$) in Fig. 4 (bottom panels) show different characteristics. On one hand, the Hα flux-intensity shows two regions with enhanced flux at nearly symmetric positions with respect to the minor photometric axis (north-east to south-west direction). These roughly correspond to the brightest star-forming clumps seen in the *HST* image (Fig. 1 middle). On the other hand, the map of $\mathrm{F}_{\mathrm{per\ cent}}$ is depressed in the nuclear region ($\mathrm{F}_{\mathrm{per\ cent},c} = 12 \pm 9$, Table 2) with respect to that of the main disc ($\mathrm{F}_{\mathrm{per\ cent,\ avg}} = 46 \pm 24$, Table 2).

The map of the log([N II]/Hα) is rather homogenous (Fig. 4 bottom) except two evident substructures. One is located towards the south-west with negative values, i.e. log([N II]/Hα) ~ -0.6, roughly at the same location of one of the regions of low velocity dispersion (region 6 in Fig. 12). The other is along the minor axis of the putative disc rotation towards north-east and south-west direction (partially overlapping the regions where velocity dispersion is enhanced, Fig. 4 top-right) and there log([N II]/Hα) is ~ 0.1. Outside the nuclear region, the distribution of the line ratios has an average value -0.35 (Fig. 7 left); the standard deviation is 0.14 (Table 2).

5.2 Second narrow component

The kinematics (velocity and velocity dispersion) of the second component (Fig. 5, top panels) have a complex shape, but, overall,

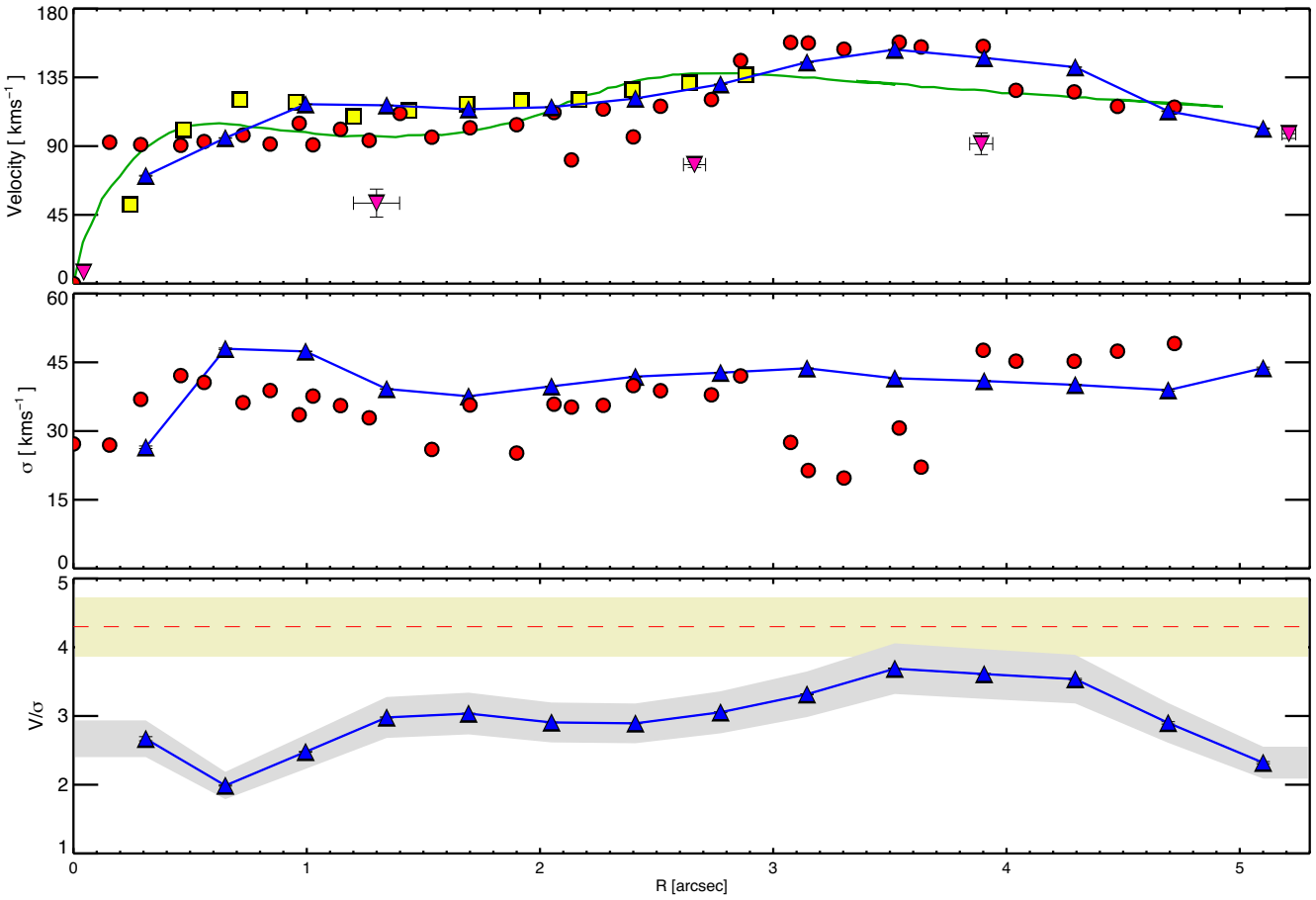

Figure 11. Rotation curve, velocity dispersion profile, and dynamical ratio distribution as a function of the distance from the photometric centre for the narrow component. In all panels, blue triangles mark the values obtained from our kinemetric analysis (Section 4.2). In the top panel, red circles indicate the rotation curve in MEGARA datacube calculated from the symmetrized rotation curve in the bottom right-hand panel of Fig. 8 (see also Section 4.1). Other symbols are from previous works (adapted for comparison purposes). Specifically, magenta upside down triangles indicate the Hα rotation curve extracted from the PV curve presented by Marquez & Moles (1994) (their fig. 12a); green continuous line corresponds to the model to the CO inclination-corrected rotation curve by Davies et al. (2004) and yellow squares represent the best-fitting to the rotation curve of the HCN emission measured by Fathi et al. (2015). Rotation curve by Müller-Sánchez et al. (2011) and Hicks et al. (2009) cover only the innermost 1.5 arcsec, thus are not considered in this figure. In the middle panel, the velocity dispersion radial profiles are from MEGARA data (red circles, Section 4.1) and from the KINEMETRY modelling (blue triangles, see also Fig. 10). In the bottom panel, the dashed line indicates the global dynamical ratio (V/σ = 4.3) estimated in Section 6.3. The shaded yellow and grey bands indicate the positions for which the dynamical ratio is equal to the ±10 per cent of its value.

Table 2. Main properties of the different components of NGC 7469.

Component	ΔV km s^{-1}	PA$_{maps}$ degree	σ_c km s^{-1}	σ_{avg} km s^{-1}	F$_{\%,c}$	F$_{\%,avg}$	log([N II]/Hα)$_c$	log([N II]/Hα)$_{avg}$
Narrow	163 ± 1	125 ± 10	40 ± 1 (15)	38 ± 1 (12)	12 ± 9	46 ± 24	−0.32 ± 0.01 (0.11)	−0.35 ± 0.02 (0.14)
Second	137 ± 2	120 ± 15	101 ± 2 (21)	108 ± 4 (42)	29 ± 12	44 ± 12	−0.18 ± 0.01 (0.11)	−0.25 ± 0.02 (0.11)
Intermediate	–	–	388 ± 5 (137)	276 ± 8 (100)	29 ± 8	32 ± 8	−0.34 ± 0.02 (0.21)	−0.10 ± 0.02 (0.10)
Broad	–	–	1100 ± 10 (156)	–	41 ± 7	–	–	–

Note. Summary of the main kinematics properties. 'ΔV' is the peak to peak semi-amplitude of the velocity field. 'PA$_{maps}$' is the position angle of the kinematic major axis, as measured from the north (anticlockwise), in the MEGARA maps. 'σ_c' ('σ_{avg}') is the average velocity dispersion calculated from the observed velocity dispersion in (excluding) the nuclear region (Section 2). Similarly, but considering the percentage-fraction (F$_{\%}$) and logarithm of [N II]/Hα, in the last columns. In parenthesis, we report the standard deviation values. Uncertainties correspond to the median value in the error-maps except for F$_{\%}$ for which it coincides with the standard deviation.

these maps suggest the presence of an irregular disc. Specifically, the ionized gas velocity map of the second narrow component seems to show both blue and red sides similarly to the spider-pattern expected in the case of a rotation-dominated system. The deviations from an ideal rotating disc include poorly defined kinematic axes, and asymmetric velocity distribution in the receding side (positive velocities) with respect to the, more regular, approaching side (negative velocities) of the putative disc. The differences in the 'regularity' between the two sides of the disc are visible in the symmetrized rotation curve in Fig. 8 (bottom right). For example, the drop of about 50 km s^{-1}

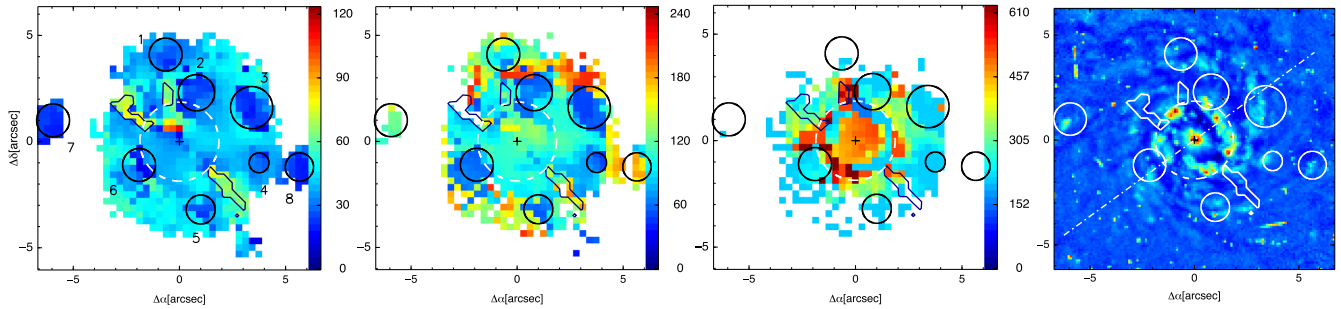

Figure 12. From *left* to the *right*: the velocity dispersion maps for the narrow, second, and intermediate components (see Section 5) and the *HST* sharp-divided image (see also Fig. 1). In all the maps the eight selected regions to be velocity dispersion anomalies (with $\sigma < 60\,\mathrm{km\,s^{-1}}$) are indicated with circles (Section 6.4). These are labelled (left-hand panel) in a clockwise pattern and considering their distance to the centre (cross). Three iso-σ contours mark the anomalies with enhanced velocity dispersion (with $\sigma > 60\,\mathrm{km\,s^{-1}}$) along the minor axis of rotation and outside the nuclear region. See Section 6.4 for details about all the σ-features. The white dashed circle marks the nuclear region, as e.g. in Fig. 4. Velocity dispersion maps are in $\mathrm{km\,s^{-1}}$ units. The white dot-dashed line marks the photometric major axis as in Fig. 4.

is visible only in the receding side. Moreover, contrary to what it is expected for a rotating disc, the velocity dispersion is not centrally peaked, with evident irregularities at large radii, i.e. $r > 3.5$ arcsec to the north-west. The distribution of the velocity dispersions is flat with $\sigma_{\mathrm{avg}} \sim \sigma_{\mathrm{c}}$ (Table 2) but with the lowest values ($< 40\,\mathrm{km\,s^{-1}}$) at a $r > 2$ arcsec. Interestingly, five out of the eight regions with the lowest velocity dispersion values for the narrow component (Section 5.1) seem to have a counterpart also in the velocity dispersion map of the second component where $\sigma < 50\,\mathrm{km\,s^{-1}}$ (Fig. 5, top right).

As mentioned above, the velocity field shows some perturbations (particularly in the red-side with positive velocities, Figs 5 top left and 8 bottom right) deviating from the putative rotating disc-like pattern. Nonetheless, the PV curve is nearly symmetric flattening at $140\,\mathrm{km\,s^{-1}}$ (Fig. 8, top right), after a shallow rise. Note that this curve has been calculated after excluding the three spaxels with very blue shifted velocities in the nuclear region, as these clearly deviate from the main rotation-like pattern of the velocity field (due to a not fully satisfactory line modelling, Section 3.1).

The Hα flux-intensity is rather homogenous and centrally peaked. The dominating feature in the percentage contribution map is the sharp drop (of about 15 per cent) towards the nuclear region (Table 2).

The map of $\log([\mathrm{N\,II}]/\mathrm{H}\alpha)$ (middle lower panel in Fig. 5) is less homogenous than the corresponding Hα flux map (Fig. 5, bottom left). The lowest values, i.e. $\log([\mathrm{N\,II}]/\mathrm{H}\alpha) \sim -0.4$, are concentrated in the north-west area. Outside the nuclear region, the distribution of the line ratios has an average value -0.25 (Fig. 7 centre); the standard deviation is 0.11 (Table 2).

5.3 Intermediate component

The velocity and velocity dispersion maps of the intermediate component, shown in the top panels of Fig. 6, are irregular, somewhat chaotic, and lack of any rotating-disc feature.

Overall, the velocity distribution is skewed to negative (blueshift) velocities. Combining the informations from both kinematic maps (velocity and velocity dispersion), we can characterized three spatially distinct regions with different kinematic properties. Outside the nuclear region, on the one hand, a region at nearly the systemic velocity, $\pm 100\,\mathrm{km\,s^{-1}}$, with a moderately high velocity dispersion ($< 300\,\mathrm{km\,s^{-1}}$). On the other hand, extreme blue shifted velocities ($V < -200\,\mathrm{km\,s^{-1}}$) correspond to an enhancement of velocity dispersion ($> 400\,\mathrm{km\,s^{-1}}$). The former has an irregular morphology and it is observed at a distance of ~ 2.5 arcsec from the photometric centre, while the latter has a ring-like morphology with a radius of ~ 1.7 arcsec. Leaving aside these two regions, the nuclear region (see Section 2) shows an intermediate kinematics with respect to the other two regions, with rest-frame velocities (between -90 and $10\,\mathrm{km\,s^{-1}}$) but high velocity dispersion, $388 \pm 5\,\mathrm{km\,s^{-1}}$ (Table 2).

The Hα flux-intensity is strongly centrally peaked (Fig. 6 bottom left). The map of $\mathrm{F}_{\mathrm{per\ cent}}$ (Fig. 6 bottom right) is rather regular (nearly ~ 30 per cent in the entire FoV, Table 2) in comparison to that of narrower components (Figs 4 and 5).

The map of the $\log([\mathrm{N\,II}]/\mathrm{H}\alpha)$ is not homogenous but not clear structures are seen (Fig. 6 bottom). Outside the nuclear region the distribution of the line ratios has an average value -0.10 (Fig. 7 right); the standard deviation is 0.10 (Table 2).

5.4 Broad component

The broad Hα component is the dominating component in the nuclear region where $\mathrm{F}_{\mathrm{per\ cent},\,c} = 41 \pm 7$ (Table 2). It is originated in the unresolved AGN's BLR.

For this component, we measured velocities that are typically rest frame, within $\pm 90\,\mathrm{km\,s^{-1}}$, with respect to the systemic. Overall, the average velocity dispersion is $\sigma_{\mathrm{c}} = 1100 \pm 10\,\mathrm{km\,s^{-1}}$ (Table 2), i.e. $\sim 2590\,\mathrm{km\,s^{-1}}$ in FWHM.

6 DISCUSSION

6.1 Comparison with previous Hα broad component measurements

Most of the previous optical studies of the BLR in NGC 7469 are focused on measurements of the FWHM of the Hβ λ4861 line from reverberation mapping campaigns (e.g. Peterson et al. 2004, 2014) with only a few direct estimates (e.g. Du et al. 2014). These works provide a range of the FWHM(Hβ) between $1967\,\mathrm{km\,s^{-1}}$ (Du et al. 2014) and $2169 \pm 459\,\mathrm{km\,s^{-1}}$ (Peterson et al. 2014). The unique measurement of the FWHM of the, less studied, Hα broad component is $1615 \pm 119\,\mathrm{km\,s^{-1}}$ from long-slit spectroscopy

data at spectral resolution of ∼9 Å (*'AGN Watch project'*, Peterson et al. 2004 and Bentz & Katz 2015 and references therein). All these previous measurements are narrower compared to that from MEGARA data in this work, i.e. ∼2590 km s^{-1} on average (see Section 5.4). This could be explained in terms of spectral resolution. The unprecedented spectral resolution of MEGARA allows a multicomponent modelling of the Hα-[N II] blend (not accounted for in previous works), that results in a more accurate estimation of the line parameters, such as the FWHM, of each component, including the broad one from the BLR. Another possibility for explaining the differences in the FWHM of the broad component is AGN variability. Pronik (2009) reviews a compilation of published data along with those available in literature (1975 – 2006) for NGC 7469 showing flux variability of the BLR (in time scales of ∼20 d or less, see also Baldi et al. 2015 and Pronik 1976). On the basis of the dramatic spectral-variability of the optical emission line profiles (fading and raising of the Hβ broad component), NGC 7469 has been classified as 'changing-look' AGN by Chuvaev, Lyutyj & Doroshenko (1990).

In order to address the variability scenario, we degraded the nuclear spectrum, i.e. that extracted at the photometric centre, from the MEGARA datacube (at reciprocal linear dispersion of ∼0.0974 Å per pixel, Section 2) to the resolution of ∼9 Å (Peterson et al. 2004; Bentz & Katz 2015). By modelling the Hα-[N II] emission in the new low-resolution nuclear spectrum with two Gaussian components (narrow + broad, as in Section 3.1), we found the broad component to have a FWHM of about 2100 km s^{-1} which is consistent with the variability hypothesis.

Thanks to MEGARA observations, we also provide the first estimate for the percentage contribution of the broad AGN component to the total Hα-[N II] profile (i.e. 41 ± 7 per cent, Table 2) which is dominant in the nuclear region.

6.2 Disc kinematics

For both narrow components, the kinematic major axes are well aligned with that of the photometric axis as seen in the *HST* images (Fig. 1) with $PA_{maps} \sim PA_{phot}$ (Tables 1 and 2, Section 5.1).

Although the velocity fields of the two narrow components show an overall similar rotation pattern, with blueshifts to the south-east and redshifts to the north-west (Figs 4, 5 and 8), it can be clearly seen that the two components present somewhat distinct kinematics in terms of velocity amplitude and velocity dispersion (Table 2). Moreover, the PV and rotation curves for the narrow and the second components show distinct shapes (Fig. 8) suggesting possible lags in velocities, besides the peak-to-peak velocities are similar (Table 2). In terms of the velocity dispersion, for both narrow components the spectral maps (Figs 4 and 5 top right) are irregular and not centrally peaked, hence they deviate from what is expected in the case of rotating discs (Section 5.1).

For the narrow component, the rotation curves derived from our MEGARA data in Fig. 11 (top panel, blue triangles and red circles) indicates a good agreement with those from past works, although the differences in the spatial coverage and ISM gas phases considered. Indeed, previous studies of NGC 7469 at optical, radio, and NIR wavelengths have shown an overall rotation-dominated kinematics of the ionized and molecular gas (Hicks et al. 2009; Müller-Sánchez et al. 2011; Fathi et al. 2015). Nevertheless, asymmetries and perturbations of the rotation curve of the galaxy and the existence of distinct kinematics components have also been observed (e.g. Marquez & Moles 1994; Davies et al. 2004). In Section 6.2.1, a detailed comparison between the results from present MEGARA IFS data and previous works is presented.

Overall, the velocity field of the narrow component has intermediate properties between *regular rotators* (i.e. $k_5/k_1 < 0.04$) and *non-regular rotators* (i.e. $k_5/k_1 > 0.04$) according to the scheme proposed by Krajnović et al. (2011) with an average value of k_5/k_1 of ∼0.04. Moreover, there is not indication of a kinematic twist (the standard deviation of the values of Γ is $< 10^{\circ}$) or other complex kinematic features such as counter rotating cores or kinematically distinct cores (Krajnović et al. 2011).

For the narrow component, the average velocity dispersion of the disc, 38 ± 1 km s^{-1} (Table 2), is in fair agreement with the spectroscopic measurements by Epinat et al. (2010), i.e. $\sigma \sim 15$–30 km s^{-1} (GHASP survey) suggesting that NGC 7469 share a similar dynamical status with local spirals. Although, this is not the case for the second component. The average velocity dispersion of the disc, 108 ± 2 km s^{-1} (Table 2), indicate a much thicker disc than in normal spirals or than the one traced by the narrow component being also larger than the typical value found at high-z, i.e. $\sigma \sim 60$–90 km s^{-1} (Förster Schreiber et al. 2011).

The reconstructed KINEMETRY map (Fig. 9 right) is rather flat displaying a drop of ∼25 km s^{-1} in the innermost region ($r \leq 1.5$ arcsec). The velocity dispersion profile from MEGARA data shown in the middle panel of Fig. 11 (red circles) is rather flat with values between 15 and 50 km s^{-1}. The two main features are: the absence of a central peak (expected for regular rotating discs) and the decrease at ∼3.3 arcsec from the nucleus. The former feature is discussed in what follows along with the results from our disc modelling (Section 4.2). The latter feature is due to the presence of two regions with low velocity dispersion (see also Fig. 5 top) located along the major axis of the rotation (hence within the psuedoslit, Section 4.1). These are regions 3 and 6 in Fig. 12, for further details see Section 6.4.

The velocity dispersion decrease at $r \leq 1.5$ arcsec (seen in both tests with KINEMETRY, Section 5.1) could indicate the presence of a σ-drop. This feature is related to dynamically cold gas (having relatively low σ) funnelled from the outer regions to the nucleus by a bar during a fast episode of central gas accretion. From this gas a young stellar population is born with similar velocity dispersion as the accreted gas. This scenario, theoretically modelled by Wozniak et al. (2003), is a rare phenomenon mostly observed for the stellar kinematics of few nearby spirals (e.g. Emsellem et al. 2001; Márquez et al. 2003; Comerón, Knapen & Beckman 2008; da Silva, Steiner & Menezes 2018). We propose that the σ-decrease of ∼25 km s^{-1} in the inner $r \leq 1.5$ arcsec of NGC 7469 could be associated to the σ-drop phenomenon, probing the low-dispersion gas funnelled by the bar. So far, in literature there are no previous cases of σ-drop observed for the ionized gas kinematics. This detection has been possible only thanks to the exquisite spectral resolution of MEGARA. To confirm this hypothesis, we search for previous estimates of the stellar kinematics with special emphasis on velocity dispersion radial profiles. We find that the unique measurements of the velocity dispersion of stars for NGC 7469 is by Onken et al. (2004). They measured the kinematics using the Ca triplet at 8498, 8542, and 8662 Å from long-slit spectroscopic low-resolution data from Kitt Peak National Observatory and MDM Observatory (60 and 90 km s^{-1} resolution, respectively). The velocity dispersion value is 152 ± 16 km s^{-1}, which is larger with respect to all the measurements for both narrow components. Their data do not either confirm or discard the σ-drop scenario. To this aim, a spatially resolved study of the stellar kinematics at high resolution is required.

6.2.1 Detailed comparison between the results from present MEGARA IFS data and previous works

For the ionized gas, Alonso-Herrero et al. (2009) modelled the Hα-[N II] lines using a broad and a narrow component in IFS observations obtained with PMAS in the LARR mode (1 arcsec magnification, V300 grating with a reciprocal linear dispersion of 1.67 Å pixel^{-1} and $R \sim 1000$) over a 16 arcsec $\times$ 16 arcsec field of view. They report a velocity curves ranging from -110 to $+207$ km s^{-1} (hence ΔV is ~ 159 km s^{-1}). This estimate is in agreement, within uncertainties, with our measurement for the narrow component. The ionized gas velocity dispersion map by Alonso-Herrero et al. (2009) strongly departs from the description of a rotating disc being chaotic. Their measurement of σ_c (125 ± 16 km s^{-1}) is very different with respect to our estimate for the narrow component but similar to that of the second component (Table 1).

The shape of PV curve of the second component is rather similar to that in Marquez & Moles (1994) obtained from slit spectroscopy of the Hα-[N II] emission. The corresponding rotation curve, adapted from their fig. 12a, is shown in Fig. 11 (magenta triangles). From the same figure we also estimated the peak-to-peak velocity amplitude being of ~ 113 km s^{-1}. This estimate is lower than our measurements for both narrow and second components (Table 2). This difference could be partially due some perturbations of the rotation curve, especially relevant at $r \geq 7$ arcsec in the approaching side of the rotating disc (negative velocities).

At near-IR wavelengths, the ionized gas kinematics have been derived from the analysis of the Brγ λ2.165 µm emission line with SINFONI/VLT and OSIRIS/Keck IFS data by Müller-Sánchez et al. (2011) in the innermost region (less than 1 arcsec $\times$ 1 arcsec) at spatial scales of ~ 0.04 arcsec ($\sim$15 pc). These authors fitted the observed Brγ line profile with a single component finding that the ionized gas velocity dispersion is on average 90 ± 9 km s^{-1} (150 km s^{-1} at maximum) and its velocity field is dominated by rotation. The same data set has been used by Hicks et al. (2009) with the aim of studying the spatial distribution, kinematics, and column density of the hot molecular gas traced by the H_2 emission line (1-0 S(1) at 2.12 µm) in a sample of nearby Seyferts with special emphasis on the correlation of the molecular gas with star formation and AGN properties. For the case of NGC 7469, they found ordered rotational motions (e.g. no warps) typical of disc kinematics and a low velocity dispersion (about 60–90 km s^{-1}). The latter varies homogeneously over the field of view being not centrally peaked. These results are similar to those measured by Fathi et al. (2015), Davies et al. (2004), Izumi et al. (2015) for the cold molecular gas. In particular, for HCN and CO $J(2 \rightarrow 1)$, the rotation curves flatten at ~ 130 km s^{-1} (Fathi et al. 2015; Davies et al. 2004, see also green line and yellow squares in Fig. 11) with a typical velocity dispersion of 60 and 22 km s^{-1}, respectively. However, all these findings are not fully comparable with those presented in this work as they strongly differ in terms of type of spatial scale, field of view and spectral resolution (e.g. a factor 5–6 higher to that of SINFONI and OSIRIS).

6.3 Dynamical support and disc height of the narrow components

The comparison of the dynamical ratio (V/σ) between the velocity amplitude and the disc velocity dispersion for the different components allow us to study the different levels of dynamical support. Specifically, the rotational support can be inferred from observed (i.e. no inclination corrected) velocity-to-velocity dispersion ratio, calculated as the ratio between the amplitude and the mean velocity dispersion across the disc (ΔV and σ_{avg} respectively, Table 2). We found that the narrow component has a rotation-dominated kinematics (V/$\sigma = 4.3$) while the second one has an increasingly larger random-motion component (V/$\sigma = 1.3$). Hence, the low rotational support of the second component is compensated by the large random motions observed and it is suggestive of a thicker, dynamically hotter disc.

In Fig. 11 (bottom panel), we show the radial profile of the dynamical ratio (i.e. V/σ) calculated using the kinemetric coefficients resulting from our disc modelling of the velocity field of the narrow component (Section 4.2 and Fig. 10). At all radii, V/σ is larger than 2 (the average is 3) suggesting a constant rotational support. The maximum of the V/σ radial profile is 3.7 being consistent, within 16 per cent, with the global dynamical ratio estimation using MEGARA kinematic maps. This value is reached at ~ 3.5 arcsec, the distance where the PV curve of the narrow component starts to flatten (Fig. 8 left).

Using optical images and IFU (FLAMES/GIRAFFE) observations Flores et al. (2006) defined three kinematical classes. Briefly these are: *rotating discs*: are characterized by a rotation in the velocity field that follows the optical major axis and the σ-map shows a clear peak near the galaxy centre; *perturbed discs*: the axis of rotation in the velocity field follows the optical major axis, and the σ-map shows a off-centred peak or no clear peak; and *complex kinematics*: system with both kinematic maps that are discrepant to normal rotation discs, and the velocity field is not aligned with the optical major axis. Accordingly to this simple scheme, both ionized discs in NGC 7469 would be ascribed to the *perturbed discs* class, as the kinematic and photometric axis are nearly coincident (Section 6.2) but velocity dispersion map are not centrally peaked (Sections 5.1 and 5.2).

This classification has been recently used by Bellocchi et al. (2013) to classify the kinematics of ionized gas discs in U/LIRGs. For LIRGs, as NGC 7469 ($\log(L_{IR}/L_\odot) = 11.7$, Table 1), the mean (median) value of the dynamical ratios is 3.4 (3.3). Considering both LIRGs and U/LIRGs classified as 'rotating disc' and 'complex kinematics', the dynamical ratios (V/σ) are 4.7 and 3.1, respectively. As for comparison, high values of V/σ (> 3) are typical of local spirals (Arribas et al. 2008), and lower V/σ values are found for more distant Lyman break analogues (i.e. V/$\sigma \leq 1.1$, Gonçalves et al. 2010) or thick neutral gas discs in U/LIRGs (i.e. V/$\sigma \leq 2.5$, Cazzoli et al. 2016).

Assuming, as in Cazzoli et al. (2014), that the narrow components are distributed in a thin (ionized gas) rotating disc and the velocity dispersion is mainly due to the gravitational potential rather than turbulence, an upper limit to the scale height of the disc (h_z) can be derived as $h_z = \sigma^2 \times R/(V(R))^2$ (Cresci et al. 2009). Considering the inclination corrected semi-amplitude, $V(R)$,[8] and the mean velocity dispersion across the disc (σ_{avg}, Table 2), heights of 20 and 222 parsecs are obtained for the discs traced by the narrow and second components, respectively. These correspond to a distance of $R = 4.3$ arcsec (i.e. 1.43 kpc, at the adopted distance, Table 1), which is the maximum radius we mapped in the MEGARA cube (Figs 4 and 5). At this distance, both PV curves nearly flatten (Fig. 8).

[8]The values of V(R) for narrow and second components are 324 and 274 km s^{-1}, respectively. These correspond to the ΔV (Table 2) corrected by inclination (i, Table 1).

Previous works about ionized gas kinematics in NGC 7469 (see Section 6.2.1) do not include measurements of both the dynamical ratio and disc height, except the work done by Hicks et al. (2009) for the warm molecular gas traced by the H_2 emission. Although we do not expect a one-to-one correspondence of the ionized and molecular discs, we found that the estimate of V/σ for the second component is fairly consistent with the previous measurements by Hicks et al. (2009) (see also Section 6.2.1). These authors found a low central V/σ ($\sim$0.5) indicating that random motions are prominent in the inner region ($r \sim 35$ pc) of NGC 7469. At slightly larger distances, i.e. $40 \leq r \leq 140$ pc, V/σ seems to be constant ($\sim$1.0). Nevertheless, their estimate of the disc height strongly differs with ours, being of the order of 30–40 pc (Hicks et al. 2009). This discrepancy could be either intrinsic (due to the mapping of two different discs, molecular versus ionized) or to the different assumptions used. They considered the two cases of a disc of self-gravitating stars and gas where the surface density (derived from their estimate of the dynamical mass) is constant and an isothermal disc for which V/$\sigma \sim r/h_z$. The latter correspond to the thick-disc approximation used in Cresci et al. (2009) (see also Cazzoli et al. 2014, 2016). We can consider that the thick disc approximation is more suitable for inferring h_z for the disc traced by the second component as dynamically hotter (likely thicker). In this scenario, an upper limit to h_z is hence 564 pc.

The height of the ionized (this work) and warm molecular (Hicks et al. 2009) discs are well below the measurements of h_z for the thin stellar disc of our Galaxy. As a reference, the stellar thin (thick) disc in the Milky Way has a scale height of $\sim$200–300 pc ($\sim$1.4 kpc) but with a (much) lower vertical velocity dispersion $\sim$20 km s^{-1} ($\sim$40 km s^{-1}), as reported by Glazebrook (2013). We would like to note that the thickness of the very-thin disc in NGC 7469 is comparable to that of the 'nuclear stellar disc' of the Milky Way which have a scale height of 45 ± 5 pc (see Nishiyama et al. 2013 and Schödel et al. 2014 for details).

Considering all this, we have found that the ionized gas in NGC 7469 is distributed in two discs. The one probed by the narrow component is a very thin disc mainly supported by rotation, in contrast, that traced by the second component is thicker and also dynamically hotter.

The turbulence, due to the increasing importance of random motions, may result from rapid accretion, disc instabilities, stellar feedback, or possibly thin-disc heating (Elmegreen et al. 2017 and Yoachim & Dalcanton 2008 and references therein). An alternative origin for the presence of the thickest ionized disc in NGC 7469 is extraplanar diffuse ionized gas gravitationally bound and virialized (e.g. Levy et al. 2018). Ancillary data, at similar spectral and spatial resolution, to study the stellar and cold gas kinematic are required to discriminate between these two scenarios.

6.4 Velocity dispersion anomalies

As mentioned in Sections 5.1 and 5.2, and 6.2, the kinematic maps for the narrow components in Figs 4 and 5 present indications of the presence of perturbations/deviations of the main disc-like kinematics, especially seen for the velocity dispersion. More specifically, these 'velocity dispersion anomalies' can be of two different kinds. On the one hand, the velocity dispersion maps of both narrow components reveal a few decrements with clump-like morphology. On the other hand, a velocity dispersion enhancement along the minor photometric axis is found only in the σ-map of the narrow component. All these features are marked in Fig. 12.

Table 3. Average values of velocity dispersion and flux ratio measured at kinematic perturbed regions.

Component	Narrow		Second	
Region	σ km s^{-1}	log ([N II]/H α)	σ km s^{-1}	log ([N II]/H α)
1	26 (3)	− 0.40 (0.04)	87 (15)	− 0.28 (0.06)
2	23 (3)	− 0.16 (0.05)	58 (5)	− 0.34 (0.03)
3	22 (4)	− 0.36 (0.06)	51 (5)	− 0.36 (0.03)
4	27 (4)	− 0.33 (0.07)	53 (9)	− 0.44 (0.03)
5	26 (3)	− 0.39 (0.05)	57 (3)	− 0.39 (0.01)
6	20 (6)	− 0.35 (0.63)	57 (3)	− 0.32 (0.03)
7†	22 (3)	− 0.44 (0.03)	116 (10)	− 0.26 (0.03)
8†	22 (4)	− 0.44 (0.03)	143 (40)	− 0.18 (0.004)

Note. Regions are marked and numbered in Fig. 12 left; † mark those regions outside the main galaxy disc. In parenthesis the standard deviation.

The first kind of anomalies correspond to eight regions (six in the main disc) where the typical velocity dispersion is lower with respect to those measured either in the central region or in the main disc (Table 2). More specifically, the velocity dispersions reach values of about $\sigma \sim$20–30 km s^{-1} and $\sim$40–60 km s^{-1} for the narrow and second component, respectively. These regions with low-σ marginally overlap with morphological features as clumps of enhanced H α emission outside the star forming ring (Figs 1 and 12 right).

A similar behaviour has been already seen for four galaxies NGC 2844, NGC 4245, NGC 5953, and NGC 774 by Falcón-Barroso et al. (2006). In their work, where they analyse the H β emission in IFS data from SAURON in its low-resolution mode (which delivers a spectral resolution of 4.2 Å in FWHM) attached to the 4.2 m William Herschel Telescope (WHT), they found low values ($\leq$40 km s^{-1}) of σ(H β) at the location of the star-forming ring (bright in H β). More recently, this behaviour has been observed by Shin et al. (2019) in high spatial resolution VLT/MUSE observations of NGC 5728.

The regions with a velocity dispersion decrement are identified and numbered in the σ-maps of the narrow component, see Fig. 12 left (circles). The main selection criteria were: to have low velocity dispersion (i.e. $\sigma < 30$ km s^{-1}), and to be clearly defined in spatial extension (i.e. with more than six neighbouring spaxels). Sizes are between $\sim$1 and $\sim$2 arcsec (i.e. 327 and 655 pc, respectively, at the adopted distance, Table 1) in diameter. The selection was not intended to match the star-forming clumps clearly visible in *HST* sharp-divided image (Fig. 1), as these are not all clearly visible in the flux maps obtained with MEGARA (Figs 4 and 5, bottom right).

Table 3 reports the average values of velocity dispersion and log ([N II]/H α) for each of the selected regions (circles in Fig. 12). These measurements are generally homogenous with regions 1, 7, and 8 deviating the most in terms of both velocity dispersion and line ratio. Regions 7 and 8, located outside the main galaxy disc, seem to have a counterpart in the *HST* image (Fig. 12) while it is not the case for region 1. If these three regions are excluded, average values for velocity dispersion and log ([N II]/H α) line ratios are: 24 (55) and − 0.32 (− 0.37) for narrow (second) component, respectively. These typical values of velocity dispersions for both components at the location of each kinematic perturbation are in agreement with those obtained in previous works by studying circumnuclear star-forming regions. For example, in the case of NGC 3351, Hägele et al. (2007) found that the H β line profiles observed in slit-spectroscopic data from the Intermediate dispersion

Spectrograph and Imaging System (ISIS) on the WHT are well described by two kinematic components with different velocity dispersions, specifically 16–30 and 43–65 km s^{-1}. Similar velocity dispersion values are observed in the circumnuclear star-forming regions of other galaxies, e.g. NGC 7479 and NGC 6070 (Firpo et al. 2010, $\sigma \sim 34-65$ km s^{-1}), as well in samples of either dwarf (Moiseev & Lozinskaya 2012, $\sigma \leq 40$ km s^{-1} generally) or interacting and isolated galaxies (Zaragoza-Cardiel et al. 2015, $\sigma \leq 60$ km s^{-1} typically).

Except two cases (regions 2 and 8 for narrow and second components, respectively), the log([N II]/H α) line ratio is generally well below −0.2. This value could be considered a reference for discriminating between ionization from AGN and from star formation (Kauffmann et al. 2003; Kewley et al. 2006; see Section 6.6).

All together these measurements seem to suggest that five out of eight regions (i.e. regions from 2 to 6, Fig. 12) could be associated to the star-forming clumps observed in NGC 7469 but unresolved in our MEGARA observations. These clumps are producing some perturbations of the overall velocity dispersion maps, but not in the velocity field. This could indicate either a high level of turbulence in these regions or that these are not fully coplanar with the thin rotating disc of NGC 7469.

Nevertheless, we recall that there is not a one-to-one correspondence between the perturbed regions identified in the MEGARA maps and star-forming regions visible in the *HST* image (Fig. 12).

For the second kind of anomalies, excluding the nuclear region, velocity dispersions are in the range between 60 to 80 km s^{-1} along the minor photometric axis (iso-σ contours in Fig. 12). At these locations, log ([N II]/H α) varies between −0.39 and −0.15 (− 0.27, on average; standard deviation is 0.07 dex). Given the observed line widths and line ratios, we suggest that these anomalies are related to either star-formation or mild-shocks (e.g. Cazzoli et al. 2018). However, the lack of counterpart in the *HST*-image makes their origin intriguing being, in any case, difficult to pinpoint with the present data set alone.

6.5 On the origin of the turbulent emission traced by the intermediate component

As mentioned in Section 5.3, the kinematic maps of the ionized gas, probed by the intermediate component, lack of any rotating-disc feature, being somewhat irregular and chaotic without any peculiar morphology (Fig. 6, top). We interpret the overall kinematics in these maps as suggestive of the presence of turbulent non-circular motions. Likely explanations for the origin of these motions are twofold.

On the one hand, these maps lack the characteristic features of outflows detected in starbursts and LIRGs with IFS (e.g. a broad and blue shifted component along the minor axis; see Cazzoli et al. 2014, 2016). Besides that, the presence of an ionized gas outflow cannot be ruled out. Indeed, recent observations of AGN-driven outflows show that these flows are detected as a broad and blue shifted component but could not be oriented perpendicular to the galaxy disc, as in the case of NGC 1068 (García-Burillo et al. 2014 and references therein). Moreover, in NGC 7469, evidences supporting the presence of an outflow have been found at other wavelengths in two previous works. The wide angle nuclear outflow detected in coronal gas by Müller-Sánchez et al. (2011) has a similar kinematics with respect to the putative one in MEGARA data, with velocity dispersion up to 250 km s^{-1} and (maximum) velocities ~ 200 km s^{-1}. At UV and X-rays multiple blue shifted outflow components have been found but with much larger velocity ($|V| \geq 580$ km s^{-1}, Blustin et al. 2007 and reference therein) than those measured in this work (Fig. 6 top).

On the other hand, the velocity and velocity dispersion maps reveal a broad ($\sigma > 450$ km s^{-1}) and blue shifted emission ($|V| < 200$ km s^{-1}) at a distance of 1.7 arcsec and extending up to 2.9 arcsec (i.e. from 580 to 990 pc at the adopted distance, Table 1). This region has an irregular and patchy ring-like morphology which is unrelated neither to that of the optical continuum or that of the flux emission of the two narrow components. The contours in the *HST* image in Fig. 12 (right) highlight that the region with high velocity dispersion is located at the outer edge of the star forming ring and it is unrelated to any bright clumps of star formation. A possible interpretation is that this turbulent gas is related to the chaotic and turbulent motions associated to gas flows at the Inner Lindblad Resonance (ILR) radius[9] of the primary large-scale lens. However, this signature could be rather faint in inclined galaxies (i.e. not edge-on), and hence difficult to detect, even more if a bright star-forming ring is present as in the case of NGC 7469.

We note that the most redshifted emission in the velocity field of the intermediate component ($V > 40$ km s^{-1}) spatially overlaps with three regions (numbered as 2, 3, and 4, Fig. 12) out of the eight regions analysed and discussed in Section 6.4. At these locations the velocity dispersion reaches ~ 200 km s^{-1}. This could be possibly explained as due to some turbulent motions outside the plane of the disc associated to these perturbations.

Leaving aside the already discussed features, a possible interpretation for the remaining emission (with $\sigma > 200$ km s^{-1}) is that it could probe some diffuse emission (possibly gravitationally bound to the host galaxy, but not virialized) outside the plane of the discs.

6.6 Line-ratios and ionization mechanisms

Standard 'BPT diagrams' (Baldwin, Phillips & Terlevich 1981) are empirically derived diagrams based on optical emission line ratios (selected to be essentially unaffected by reddening) that allow to discriminate different ionizing mechanisms. We cannot use the BPT diagrams to study in detail the possible ionization mechanism of the narrow and intermediate components found in our analysis, as the MEGARA VPH (665-HR, see Section 2), at the redshift of NGC 7469 (Table 1), covers only the H α-[N II] complex. Despite this, the values of log ([N II] λ6583/H α) give helpful limits in order to investigate the dominant mechanism of ionization.

For the following discussion, we do not exclude the regions named 'disc-perturbations' (see Section 6.4) as they are relatively small (the diameters are on average of 1.5 arcsec, 497 pc at the adopted distance, Table 1) and hence represent a minor fraction of the spaxels within the maps.

Considering the typical values of the histograms for the [N II]/H α ratio (Fig. 7, averages values are between − 0.35 and − 0.10) and the dividing lines discriminating ionization from AGN and star formation by Kewley et al. (2006) and Kauffmann et al. (2003), for all the three components line ratios suggest the ionization from star-formation as the dominant mechanism. We do not have spatially resolved information about the [O III] λ5007/H β ratio. However, as the division between AGN and star formation occurs

[9]The location of the ILR has be proposed to be likely coincident with the ring (with diameter of 3 arcsec) considering the morphology of the molecular gas, large-scale bar, optical, and radio continuum emission, and MIR-emission of young stars by Wilson et al. (1991), Marquez & Moles (1994), Davies et al. (2004), and Díaz-Santos et al. (2007).

at [O III]/H $\beta \sim 3$ (0.5 in log units), such high values of [O III]/H β, along with low levels of [N II]/H α, could have been produced only in gas with very low metallicity. This is unlikely to be the case of NGC 7469, as the high current star-formation activity[10] with possible SN explosions (the last in 2000, Colina et al. 2007) might have considerably polluted with metals the surrounding ISM.

For the narrow component the [N II]/H α ratios point to ionization from star formation. For the intermediate component, the distribution of the line ratios outside the nuclear region is skewed towards Seyfert- and LINER-like ratios (with log [N II] λ6583/H α up to 0.2 dex, Fig. 7 right). This might suggest that, given the large velocity dispersion (up to 610 km s^{-1}, on average 276 ± 8 km s^{-1}; see Table 2), shocks play a significant role in the ionization of the gas (Molina et al. 2018) and might have altered the two discs (injecting some level of turbulence). In the specific case of the second component, although the dominant ionization mechanism is star formation, with log ([N II]/H α) < -0.2 generally, for a minor fraction of the data points (35 per cent) the ratios are between -0.2 and 0.2 dex suggesting a mixture of star formation, shock excitation, and AGN activity. In these particular cases, the knowledge of [O III]/H β is essential to pin-point the ionization mechanism.

The values of the [N II]/H α ratio are in partial agreement with those reported by Alonso-Herrero et al. (2009) for the integrated spectrum (i.e. 0.55, log units), with the nuclear spectrum as a complete different value (i.e. -0.26, log units). The values of the [O III]/H β ratio reported in by Alonso-Herrero et al. (2009) are 0.55 to 1 (in log units) for integrated and nuclear spectra, respectively. Although relatively high values of [O III]/H β are already observed, these cannot be used to better constraint the ionization mechanism of NGC 7469 due to the difference with our data (e.g. spectral and spatial resolution) and number of components for the modelling of narrow emission lines with respect to theirs (single versus multiple Gaussians).

Therefore, our measurements of the [N II]/H α ratio indicate the star formation as the exclusive (dominant) ionization mechanism of gas probed by the narrow (second) component in NGC 7469. For the third intermediate broader component, given the observed line widths, line ratios suggest ionization by shocks.

Optical nebular line ratios are widely exploited to constrain the metallicity in galaxies (see Maiolino & Mannucci 2019 for a review). Among them, the only calibrator that can be used with the present MEGARA data is N2 defined to be equal to the log ([N II]/H α). Overall, for the three components, considering the typical line ratios summarized in column 9 of Table 2 (outside the nuclear region in order to avoid possible AGN-contamination) and assuming the calibration by Marino et al. (2013), the oxygen abundance (12 + log(O/H)) varies from 8.58 to 8.70. These values suggest that the typical metallicity of the three components is solar (i.e. 8.69; Asplund et al. 2009).

7 CONCLUSIONS

On the basis of optical MEGARA IFS high resolution ($R \sim 20\,000$) data we have studied the properties (kinematic and dynamical as well as fluxes ratios and oxygen abundances) of the ionized gas in the Seyfert 1.5 galaxy NGC 7469, using as tracers the H α-[N II] emission lines.

[10]The ring of star formation, where supernova explosions take place, is contributing up to two thirds of the galaxy's bolometric luminosity (Fathi et al. 2015 and references therein).

The conclusions of this study can be summarized as follows:

(1) *BLR properties*. In the nuclear region of NGC 7469 ($r \leq 1.85$ arcsec) the broad ($\sigma = 1100 \pm 10$ km s^{-1}, FWHM ~ 2590 km s^{-1}) H α component is dominating (i.e contribution of 41 per cent) the global H α-[N II] profile, being originated in the (unresolved) BLR of the AGN. The unprecedented spectral resolution of MEGARA allows a multicomponent modelling of the H α-[N II] blend (not accounted for in previous works), that results in the most accurate measurements so far for the BLR-originated H α component.

(2) *Discs kinematics and classification*. The two discs, probed by the narrow and second components, nearly corotate with similar peak-to-peak velocities, 163 and 137 km s^{-1}, respectively, but with different velocity dispersion, i.e. 38 ± 1 and 108 ± 4 km s^{-1}, respectively. The analysis of their kinematic maps (velocity and velocity dispersion) led to be both classified as 'Perturbed discs' (Flores et al. 2006) since their major kinematic axis well aligned with the photometric axis, their velocity maps are fairly regular but both velocity dispersion maps deviate from the case of an ideal rotating disc. Although both components share the same disc classification, we remark that the disc traced by the second component is the most perturbed within the two, with a more disturbed velocity field and irregular PV curve.

(3) *Dynamical support and disc height*. The difference in the velocity dispersion of the two discs indicates that the disc traced by the narrow component share a similar dynamical status with local spirals, while the other, traced by the second component, is likely to be thicker and turbulent, having higher velocity dispersion with respect to both spirals and high-z star forming galaxies. We found that the very thin (20 pc) ionized gas disc, mainly supported by rotation (V/σ = 4.3), is embedded in a thicker (222–564 pc), dynamically hotter (V/σ = 1.3) one.

(4) *Discs modelling and kinemetric analysis*. We successfully modelled the kinematics of the thin ($h_z = 20$ pc) ionized gas disc with KINEMETRY (Krajnović et al. 2006). The position angle is remarkably stable (within 120° and 130°) at nearly all reconstructed ellipses, with no indication of kinematic twists, counter rotating cores or kinematically distinct cores. These values are in good agreement with literature (126°) and other estimates in this work, i.e. $(125 \pm 10)°$ from MEGARA maps and $(124.3 \pm 2.5)°$ from an alternative method by Krajnović et al. (2006). In addition, it exhibits a kinematically round velocity map with large opening angles reflected in the high values of (q), i.e. 0.88 on average, and with intermediate properties between *regular* and *non-regular rotators* (Krajnović et al. 2011) as indicated by the k_5/k_1 parameter (~ 0.04).

(5) *Ionized gas σ-drop*. We found a velocity dispersion diminution in the velocity dispersion radial profile (output of KINEMETRY), of about 25 km s^{-1} at $r \leq 1.5$ arcsec. This feature is suggestive of the presence of a σ-drop related to dynamically cold gas funnelled from the outer regions to the nucleus by a bar during a fast episode of central gas accretion. So far, in the literature there are no previous cases of σ-drop observed for the ionized gas kinematics (with few cases detected through the analysis of stellar kinematics). This detection has been possible only thanks to the exquisite spectral resolution of MEGARA.

(6) *Intermediate-width component*. The morphology and the kinematics of the third (intermediate-width) component is suggestive of the presence of turbulent non-circular motions, possibly associated either to an ionized gas wide angle outflow (oriented not perpendicular to the galaxy disc) or to gas flows related to the large-

scale lens. Part of the ionized gas traced by this component could be also due to turbulent motions outside the plane of the disc related to disc perturbations, and with diffuse ionized gas gravitationally bound to the host galaxy, but not virialized.

(7) *Ionization mechanisms and oxygen abundances*. For the narrow (second) component the [N II]/H α line ratios are indicative of star-formation as the unique (dominant) mechanism of ionization. For the intermediate component, given the observed line-widths, the [N II]/H α ratios are consistent with ionization from shocks. For all the three kinematic components our measurements suggest that the gas has roughly solar metallicity.

As a final remark, we highlight that studies of this kind of nearby galaxies at high spectral resolution represent a benchmark for the interpretation of future observations with next-generation 30 m class telescopes. For example, the European Extremely Large Telescope, will be equipped with intermediate to high resolution ($R \sim$ 3000–20 000) spectrographs such as MOSAIC and HARMONI.

ACKNOWLEDGEMENTS

This paper is based on observations made with the Gran Telescopio Canarias (GTC), installed in the Spanish Observatorio del Roque de los Muchachos of the Instituto de Astrofísica de Canarias, in the island of La Palma. This work is based on data obtained with MEGARA instrument, funded by European Regional Development Funds (ERDF), trough Programa Operativo Canarias FEDER 2014-2020.

SC, IM, JM, and LHM acknowledge financial support by the Spanish Ministry of Economy and Competitiveness (MEC) under grant no. AYA2016-76682-C3. We also acknowledge financial support from the State Agency for Research of the Spanish MCIU through the 'Center of Excellence Severo Ochoa' award to the Instituto de Astrofísica de Andalucía (SEV-2017-0709).

AGdP, JG, ACM, SP, and NC acknowledge financial support from the Spanish MEC under grant no. AYA2016-75808-R.

This research has made use of the NASA/IPAC Extragalactic Database (NED), which is operated by the Jet Propulsion Laboratory, California Institute of Technology, under contract with the National Aeronautics and Space Administration. We acknowledge the usage of the HyperLeda database (http://leda.univ-lyon1.fr).

This paper made use of the plotting package JMAPLOT, developed by Jesús Maíz-Apellániz available at: http://jmaiz.iaa.es/software/jmaplot/ current/html/jmaplot_overview.html.

The authors acknowledge the anonymous referee for her/his instructive comments that helped to improve the presentation of this paper.

SC thanks R. Amorin and R. Schödel for their useful comments.

REFERENCES

Akaike H., 1974, IEEE Trans. Autom. Control, 19, 716
Alonso-Herrero A., García-Marín M., Monreal-Ibero A., Colina L., Arribas S., Alfonso-Garzón J., Labiano A., 2009, A&A, 506, 1541
Arribas S., Colina L., Monreal-Ibero A., Alfonso J., García-Marín M., Alonso-Herrero A., 2008, A&A, 479, 687
Arribas S., Colina L., Bellocchi E., Maiolino R., Villar-Martín M., 2014, A&A, 568, A14
Asplund M., Grevesse N., Sauval A. J., Scott P., 2009, ARA&A, 47, 481
Baldi R. D., Behar E., Laor A., Horesh A., 2015, MNRAS, 454, 4277
Baldwin J. A., Phillips M. M., Terlevich R., 1981, PASP, 93, 5
Bellocchi E., Arribas S., Colina L., Miralles-Caballero D., 2013, A&A, 557, A59
Bentz M. C., Katz S., 2015, PASP, 127, 67
Blustin A. J. et al., 2007, A&A, 466, 107
Bordoloi R. et al., 2017, ApJ, 834, 191
Bosch G. et al., 2019, MNRAS, 489, 1787
Bundy K. et al., 2015, ApJ, 798, 7
Cappellari M. et al., 2007, MNRAS, 379, 418
Carrasco E. et al., 2018, in Evans C. J., Simard L., Takami H., eds, Proc. SPIE Conf. Ser. Vol. 10702, Ground-based and Airborne Instrumentation for Astronomy VII. SPIE, Bellingham, p. 1070216
Catalán-Torrecilla C. et al., 2020, ApJ, 890, 5
Cazzoli S., Arribas S., Colina L., Piqueras-López J., Bellocchi E., Emonts B., Maiolino R., 2014, A&A, 569, A14
Cazzoli S., Arribas S., Maiolino R., Colina L., 2016, A&A, 590, A125
Cazzoli S. et al., 2018, MNRAS, 480, 1106
Chen Y.-M., Tremonti C. A., Heckman T. M., Kauffmann G., Weiner B. J., Brinchmann J., Wang J., 2010, AJ, 140, 445
Chuvaev K. K., Lyutyj V. M., Doroshenko V. T., 1990, Pisma v Astron. Zhurnal, 16, 867
Colina L., Alberdi A., Torrelles J. M., Panagia N., Wilson A. S., 2001, ApJ, 553, L19
Colina L., Díaz-Santos T., Alonso-Herrero A., Panagia N., Alberdi A., Torrelles J. M., Wilson A. S., 2007, A&A, 467, 559
Comerón S., Knapen J. H., Beckman J. E., 2008, A&A, 485, 695
Cresci G. et al., 2009, ApJ, 697, 115
Croom S. M. et al., 2012, MNRAS, 421, 872
da Silva P., Steiner J. E., Menezes R. B., 2018, ApJ, 861, 83
Davies R. I., Tacconi L. J., Genzel R., 2004, ApJ, 602, 148
Díaz-Santos T., Alonso-Herrero A., Colina L., Ryder S. D., Knapen J. H., 2007, ApJ, 661, 149
Du P., Wang J.-M., Hu C., Valls-Gabaud D., Baldwin J. A., Ge J.-Q., Xue S.-J., 2014, MNRAS, 438, 2828
Dullo B. T. et al., 2019, ApJ, 871, 9
Elmegreen B. G., Elmegreen D. M., Tompkins B., Jenks L. G., 2017, ApJ, 847, 14
Emsellem E., Greusard D., Combes F., Friedli D., Leon S., Pécontal E., Wozniak H., 2001, A&A, 368, 52
Emsellem E. et al., 2007, MNRAS, 379, 401
Epinat B., Amram P., Balkowski C., Marcelin M., 2010, MNRAS, 401, 2113
Falcón-Barroso J. et al., 2006, MNRAS, 369, 529
Fathi K. et al., 2015, ApJ, 806, L34
Fiore F. et al., 2017, A&A, 601, A143
Firpo V., Bosch G., Hägele G. F., Morrell N., 2010, MNRAS, 406, 1094
Flores H., Hammer F., Puech M., Amram P., Balkowski C., 2006, A&A, 455, 107
Förster Schreiber N. M. et al., 2009, ApJ, 706, 1364
Förster Schreiber N. M. et al., 2011, ApJ, 739, 45
Fox A. J. et al., 2015, ApJ, 799, L7
Fox A. et al., 2019, Bull. Am. Astron. Soc., 51, 21
Galbany L. et al., 2016, MNRAS, 455, 4087
García-Burillo S. et al., 2014, A&A, 567, A125
Genzel R., Weitzel L., Tacconi-Garman L. E., Blietz M., Cameron M., Krabbe A., Lutz D., Sternberg A., 1995, ApJ, 444, 129
Gil de Paz A. et al., 2014, in Ramsay S. K., McLean I. S., Takami H., eds, Proc. SPIE Conf. Ser. Vol. 9147, Ground-based and Airborne Instrumentation for Astronomy V. SPIE, Bellingham, p. 91470O
Gil de Paz A. et al., 2018, in Evans C. J., Simard L., Takami H., eds, Proc. SPIE Conf. Ser. Vol. 10702, Ground-based and Airborne Instrumentation for Astronomy VII. SPIE, Bellingham, p. 1070217
Glazebrook K., 2013, Publ. Astron. Soc. Aust., 30, e056
Gonçalves T. S. et al., 2010, ApJ, 724, 1373
Hägele G. F., Díaz Á. I., Cardaci M. V., Terlevich E., Terlevich R., 2007, MNRAS, 378, 163
Harrison C. M., Alexander D. M., Mullaney J. R., Swinbank A. M., 2014, MNRAS, 441, 3306
Heckman T. M., Lehnert M. D., Strickland D. K., Armus L., 2000, ApJS, 129, 493

Hermosa-Muñoz L., Cazzoli S., Márquez I., Masegosa J., 2020, preprint (arXiv:2001.02955)
Hernández-García L. et al., 2018, MNRAS, 478, 4634
Hernández-García L. et al., 2019, MNRAS, 489, 4049
Hicks E. K. S., Davies R. I., Malkan M. A., Genzel R., Tacconi L. J., Müller Sánchez F., Sternberg A., 2009, ApJ, 696, 448
Izumi T. et al., 2015, ApJ, 811, 39
Kauffmann G. et al., 2003, MNRAS, 346, 1055
Kewley L. J., Groves B., Kauffmann G., Heckman T., 2006, MNRAS, 372, 961
Kollatschny W., Zetzl M., 2013, A&A, 549, A100
Krajnović D., Cappellari M., de Zeeuw P. T., Copin Y., 2006, MNRAS, 366, 787
Krajnović D. et al., 2011, MNRAS, 414, 2923
Landt H., Bentz M. C., Ward M. J., Elvis M., Peterson B. M., Korista K. T., Karovska M., 2008, ApJS, 174, 282
Levy R. C. et al., 2018, ApJ, 860, 92
Maiolino R., Mannucci F., 2019, A&AR, 27, 3
Maiolino R. et al., 2017, Nature, 544, 202
Maíz-Apellániz J., 2004, PASP, 116, 859
Marino R. A. et al., 2013, A&A, 559, A114
Markwardt C. B., 2009, in Bohlender D. A., Durand D., Dowler P., eds, ASP Conf. Ser., Vol. 411, Astronomical Data Analysis Software and Systems XVIII. Astron. Soc. Pac., San Francisco, p. 251
Marquez I., Moles M., 1994, AJ, 108, 90
Márquez I. et al., 1999, A&AS, 140, 1
Márquez I., Masegosa J., Durret F., González Delgado R. M., Moles M., Maza J., Pérez E., Roth M., 2003, A&A, 409, 459
Moffat A. F. J., 1969, A&A, 3, 455
Moiseev A. V., Lozinskaya T. A., 2012, MNRAS, 423, 1831
Molina M., Eracleous M., Barth A. J., Maoz D., Runnoe J. C., Ho L. C., Shields J. C., Walsh J. L., 2018, ApJ, 864, 90
Müller-Sánchez F., Prieto M. A., Hicks E. K. S., Vives-Arias H., Davies R. I., Malkan M., Tacconi L. J., Genzel R., 2011, ApJ, 739, 69
Nilson P., 1973, Nova Acta Regiae Soc. Sci. Upsaliensis Ser. V.
Nishiyama S. et al., 2013, ApJ, 769, L28
Onken C. A., Ferrarese L., Merritt D., Peterson B. M., Pogge R. W., Vestergaard M., Wandel A., 2004, ApJ, 615, 645
Osterbrock D. E., Ferland G. J., 2006, Astrophysics of Gaseous Nebulae and Active Galactic Nuclei. University Science Books, Sausalito, CA
Osterbrock D. E., Fulbright J. P., Martel A. R., Keane M. J., Trager S. C., Basri G., 1996, PASP, 108, 277
Pascual S., Cardiel N., Gil de Paz A., Carasco E., Gallego J., Iglesias-Páramo J., Cedazo R., 2019a, in Montesinos B., Asensio Ramos A., Buitrago F., Schödel R., Villaver E., Pérez-Hoyos S., Ordóñez-Etxeberria I., eds, Highlights on Spanish Astrophysics X. Spanish Astronomical Society, Salamanca, Spain, p. 227
Pascual S., Cardiel N., Picazo-Sanchez P., Castillo-Morales A. A. G., 2019b, in press
Paturel G., Fang Y., Petit C., Garnier R., Rousseau J., 2000, A&AS, 146, 19
Pereira-Santaella M. et al., 2011, A&A, 535, A93
Pereira-Santaella M. et al., 2017, A&A, 601, L3
Peterson B. M. et al., 2004, ApJ, 613, 682
Peterson B. M. et al., 2014, ApJ, 795, 149
Pronik I. I., 1976, Sov. Astron., 19, 293
Pronik I. I., 2009, A&A, 496, 299
Sánchez S. F. et al., 2012, A&A, 538, A8
Sanders D. B., Mazzarella J. M., Kim D.-C., Surace J. A., Soifer B. T., 2003, AJ, 126, 1607
Schödel R., Feldmeier A., Kunneriath D., Stolovy S., Neumayer N., Amaro-Seoane P., Nishiyama S., 2014, A&A, 566, A47
Scoville N. Z. et al., 2000, AJ, 119, 991
Shapiro K. L. et al., 2008, ApJ, 682, 231
Shin J., Woo J.-H., Chung A., Baek J., Cho K., Kang D., Bae H.-J., 2019, ApJ, 881, 147
Soifer B. T., Bock J. J., Marsh K., Neugebauer G., Matthews K., Egami E., Armus L., 2003, AJ, 126, 143
Veilleux S., Cecil G., Bland-Hawthorn J., 2005, ARA&A, 43, 769
Wei J.-J., Wu X.-F., Melia F., 2016, MNRAS, 463, 1144
Westmoquette M. S., Smith L. J., Gallagher J. S. III, 2011, MNRAS, 414, 3719
Wilson A. S., Helfer T. T., Haniff C. A., Ward M. J., 1991, ApJ, 381, 79
Wisnioski E. et al., 2015, ApJ, 799, 209
Wozniak H., Combes F., Emsellem E., Friedli D., 2003, A&A, 409, 469
Yoachim P., Dalcanton J. J., 2008, ApJ, 682, 1004
Zaragoza-Cardiel J. et al., 2015, MNRAS, 451, 1307

This paper has been typeset from a TEX/LATEX file prepared by the author.